Multi-omics comparison of malignant and normal uveal melanocytes reveals novel molecular features of uveal melanoma.

Authors:
David Gentien[1,2,*], Elnaz Saberi-Ansari[1,3], Nicolas Servant[4], Ariane Jolly[5], Pierre de la Grange[5], Fariba Nemati[1,6], Geraldine Liot[7], Simon Saule[7,8], Aurélie Teissandier[9], Deborah Bourchis[9], Elodie Girard[4], Jennifer Wong[10], Julien Masliah Planchon[10], Manuel Rodrigues[11,12], Laure Villoing Gaudé[1,2], Cécile Reyes[1,2], Emilie Henry[1,2], Sylvain Baulande[13], Radhia M'kacher[14], Eric Jeandidier[15], André Nicolas[16], Didier Decaudin[1,6], Nathalie Cassoux[10,17], Sophie Piperno-Neumann[11], Marc-Henri Stern[12], Johan H. Gibcus[18], Job Dekker[18], Edith Heard[19], Sergio Roman-Roman[1,Ω,*], Joshua J. Waterfall[1,3,Ω,*].

Affiliation:

1. Translational Research Department, Research Center, Institut Curie, Paris Sciences et Lettres (PSL) Research University, 75005 Paris, France
2. Genomics Platform
3. INSERM U830, Research Center, Institut Curie, PSL Research University, 75005 Paris
4. INSERM U900, Mines ParisTech, 75248 Paris, France
5. GenoSplice, Paris, France.
6. Preclinical Investigation Laboratory.
7. Institut Curie, PSL Research University, CNRS, INSERM, UMR3347, U1021, Orsay, France;
8. Université Paris-Saclay Centre National de La Recherche Scientifique, Unité Mixte de Recherche 3347, Unité 1021, Orsay, France.
9. INSERM U934, CNRS UMR 3215, 75005 Paris, France.
10. Department of Diagnostic and Theranostic Molecular Pathology, Unit of Somatic Genetic, Hospital, Institut Curie, Paris, France.
11. Department of Medical Oncology, Institut Curie, PSL Research University, F-75005, Paris, France.
12. INSERM U830, DNA Repair and Uveal Melanoma (D.R.U.M.), Equipe Labellisée par la Ligue Nationale Contre le Cancer, Department of Genetics, Institut Curie, PSL Research University, F-75005 Paris, France.
13. Institut Curie Genomics of Excellence (ICGex) Platform, Institut Curie Research Center, PSL Research University, Paris, France.
14. Cell Environment, DNA Damage R&D, 75020 Paris, France.
15. Laboratoire de Génétique, Groupe Hospitalier de la Région de Mulhouse Sud-Alsace, Mulhouse, France
16. Pathex, Institut Curie, PSL Research University, Paris, France.
17. Department of Ocular Oncology, Faculty of Medicine, Institut Curie, Université de Paris Descartes, F-75005 Paris, France.
18. Howard Hughes Medical Institute, and Program in Systems Biology, Department of Biochemistry and Molecular Pharmacology, University of Massachusetts Medical School, Worcester, Massachusetts 01605, USA.
19. Director's Unit, European Molecular Biology Laboratory, 69117 Heidelberg, Germany.

Ω. Co-senior Authors.

*. Correspondence: dgentien@curie.fr; sergio.roman-roman@curie.fr; joshua.waterfall@curie.fr

Summary

Uveal Melanoma (UM) is a rare cancer resulting from the transformation of melanocytes residing in the uveal tract. Integrative analysis has identified four molecular and clinical subsets in UM. To improve our understanding of UM we performed extensive multi-omics characterization comparing pure melanoma populations obtained from two aggressive UM patient-derived xenograft models with normal choroidal melanocytes. Our study addresses for the first time DNA optical mapping, specific histone mark modifications, DNA topology analysis by Hi-C. Gene expression and cytogenetic analyses suggest that genomic instability is a hallmark of UM. Our study also identified a recurrent deletion in the *BAP1* promoter which results in the absence of expression of BAP1 which is associated with high risk of metastases in UM patients. Chromatin topology changes are associated with up-regulation of PRAME, a recognized independent prognostic biomarker in UM and potential therapeutic target. Our findings illustrate how multi-omics integrative approaches can improve the understanding of tumorigenesis and reveals two novel mechanisms of gene expression dysregulation in UM.

Introduction

Uveal Melanoma (UM) is a rare cancer (5-7 cases per million per year) affecting mainly adults and represents 5% of all melanoma [1]. UM results from the transformation of melanocytes of the uveal tract of the eye, which comprises the iris, the ciliary body, and choroidal membrane [2]. UM primary tumors are well controlled by surgery and/or radiotherapy but more than 30% of the patients develop metastases, mainly in the liver, of very poor prognosis. Improvement in the understanding of aggressive UM is essential for identifying efficient new therapeutic approaches.

The vast majority of UM display activating mutations of *GNAQ* [7] or its paralog *GNA11* [8], their upstream activator *CYSLTR2* [9] or downstream effector *PLCB4* [10]. These Gα/q-related mutations present in 98% of UM are recognized as a primary event of UM oncogenesis [11] and lead to the activation of Gα/q signaling pathway. Mutations in *BAP1, EIF1AX, SF3B1,* and *SRSF2,* [12]–[14] were identified as a secondary mutational event necessary for malignant transformation. Mutations in *BAP1, SF3B1,* and *EIF1AX* (so called BSE event) are associated with distinct delays in the appearance of metastasis with earlier onset of metastasis in a BAP1 loss of function setting [15].

A number of recurrent chromosomal abnormalities have been identified in the last two decades including monosomy 3 (M3), gains of 6p and 8q, as well as loss of 6q and 8p, which are associated with clinical outcome and are currently used in clinical daily practice [3]–[6]. Monosomy 3 and gain of chr 8 correlate with an intermediate risk of metastasis and the highest risk of metastasis is associated with combined M3 and gain of 8q [4], [6]. Integrative analysis including copy number alterations, DNA methylation, recurrent mutations, and gene expression profiles has identified four molecular and clinical subsets in UM [6].

To improve our understanding of tumor oncogenesis, we performed extensive multi-omic and FISH characterization of two aggressive UM PDX with distinct mutational and chromosomal rearrangement patterns as well as short term culture of normal choroidal melanocytes (NM) for comparison. In addition to somatic DNA alterations, RNA sequencing, and DNA topology analysis, other analyses included whole genome DNA methylation sequencing and chromatin immunoprecipitation (ChIP-seq) of histone marks associated with activating (H3K4me3), repressing (H2A119Ub, H3K27me3) or enhancing (H3K27Ac) gene expression. Such complementary analysis may improve the characterization of regulated genes and pathways in aggressive UM

Results

Samples studied

The goal of this study is to improve the molecular understanding of aggressive UM by performing multi-omics analysis (including whole genome sequencing, RNAseq, DNA methylation profiling, in situ Hi-C, histone mark ChIPseq, and DNA optical mapping) of two uveal melanoma patient-derived xenograft (PDX) models from patients with aggressive disease. Importantly, to contextualize these expression and epigenetic profiles with respect to the cell of origin, we also analyzed normal uveal melanocytes from healthy donors.

To have a pure tumor population and a sufficient number of tumor cells to perform the complete set of omics technologies we sorted UM cells from two PDX models established from aggressive UM: MP41 and MP46 [3]–[5]. Clinical and mutational/copy number characteristics of these tumors are illustrated in Figure 1. The MP41 model was generated from enucleation of a primary UM occurring in a 50-year-old female patient who had a metastasis 31 months after initial diagnosis and who died 43 months after diagnosis from multiple metastases (including bones, lung, and subcutaneous metastases). The MP46 model was established from enucleation of a primary tumor occurring in a 69-year-old male patient. This patient developed a liver metastasis 6 months after diagnosis of the primary tumor, and died 7 months from initial diagnosis. These two aggressive models harbor canonical activating mutations in *GNAQ/11* genes and share 8q and 6p gains. MP46 displays monosomy of chromosome 3 and is deficient in BAP1 expression by immunohistochemistry (IHC) (Figure 1b) although no *BAP1* mutation was identified by Sanger sequencing. MP41 is BAP1 proficient by IHC (Fig 1B) and no mutations were identified in *BAP1, SF3B1* or *EIF1AX*.

Whole genome sequencing and copy number analysis confirmed MP41 and MP46 as high risk UM.

First, MP41 and MP46 were subjected to whole genome sequencing (WGS) to perform somatic mutation and a copy number analysis. To facilitate the identification of single nucleotide variants (SNVs), WGS was also conducted on uveal healthy tissue adjacent to primary tumors of the patients from whom the PDXs were established.
Somatic point mutation analysis revealed less than one somatic mutation per Mb (0.42 and 0.37 SNV/Mb) as observed in UM [6]. Based on Cancer Genome Interpreter and VarSome classification, a unique known driver mutation associated to a pathogenic role was retrieved in MP41 (*GNA11* c.626A>T, allele frequency (AF):43%) and in MP46 (*GNAQ* c.626A>T, AF: 43% AF). Supplementary Tables 1 and 2 list all the SNVs labelled as passenger mutations, having a moderate to high impact on amino acid sequence, or affecting ncRNAs for MP41 and MP46, respectively. Additional mutations identified in MP41 were composed of one predicted known driver mutation in *KMT2C* based on a stop gained (KMT2C:[p.Tyr987*]) and 13 passenger mutations (based on oncodrive MUT algorithm). Additional mutations in MP46 as 21 passenger mutations in 19 genes were annotated as passenger and pathogenic for 8 genes due to indels causing frameshift variant (insertion: *AQPEP*:[p.Ala859fs], *SGSM2*:[p.Pro732fs]; deletion: *CTDSP2*:[p.Lys212fs]; *CTBP2*:[p.Gly743fs]; *CTBP2*:[p.Gln971fs]; *CDH11*:[p.Arg137fs]), and substitutions causing stop gained mutations (*PTGFRN*:[p.Ser343*], *WDR89*:[p.Arg100*]) or splicing defects (*SACM1L*).

The comprehensive TCGA UM study distinguishes four copy number subtypes that had diverse aneuploid events and divided D3-UM and M3-UM into two subgroups each based on somatic copy number alterations [6]. Somatic copy number alterations as losses (L) and gains (G) identified from WGS of MP41 and MP46 models include for MP41: L1p, G1q, M3, G6p, L6q, L8p, G8q, L9, L10, G11q,G12p, G16p, L16q, G21, and for MP46: G1q, G2, Isodisomy 3, G6p, G7, L8p, G8q, L16q, G17, G18, L20p, G20q, G21, G22. Copy number profiles of MP41 and MP46 were attributed to group 2 and group 4 upon the TCGA classification of uveal melanomas [6]. As BAP1-deficient tumors are associated to group 4, MP46 classification is in agreement with our expectations. Although TCGA group 2 is enriched in *SF3B1*-mutated, no *SF3B1* or *SRSF2* and no *SF3B1* splicing pattern were observed in MP41[7].

Overall, whole genome sequencing analysis of MP41 and MP46 models confirmed the presence of a unique oncogenic driver mutation in the Gαq pathway, the presence of M3 and G8q, and an association of TCGA group 2 for MP41 and group 4 for MP46.

Gene expression analysis reveals upregulation of well-known genes and identifies DNA repair pathway as a potential hallmark of UM.

As a starting point of our integrative analysis, we performed a gene expression analysis to compare the transcriptome of UM models to normal choroidal melanocytes. The RNAseq dataset was composed of five normal melanocytes cell lines (NM) including a technical replicate, four MP41 biological replicates and three MP46 biological replicates.

Unsupervised analyses by principal components analysis (PCA) and hierarchical clustering of all significant regulated genes (log2FC>1.5, p-value ≤ 5%) are shown on Figure 2A and B. These demonstrate high reproducibility of the replicates as well as clear separation between UM models and NM.

To identify genes consistently differentially expressed in aggressive UM, we independently compared each PDX to the NM and then compared the resulting gene lists (Figure 2C). A total of 8,212 differentially expressed genes was identified in MP41 compared to NM including 4,149 upregulated genes and 4,063 downregulated genes (Figure 2C, Supplementary Table 1). Among the 9,368 regulated genes identified in MP46 versus NM 4,337 were upregulated and 5,031 were downregulated genes. Among the regulated genes, the tumor samples shared 3,066 downregulated genes and 2,334 upregulated genes as compared to NM. The common regulated genes were subjected to further analyses.

Cancer testis antigens were significantly enriched among the consistently upregulated genes in MP41 and MP46, with *PRAME* [8] as the highest cancer testis antigen expressed in both MP41 and MP46 (log2 fold change: ~12). Two genes described as key players in UM oncogenesis were among the top 50-upregulated genes, *PLCB4* and *RASGRP3*. A small percentage of UM patients display activating mutations in the PKC regulator *PLCB4* which are mutually exclusive with *GNAQ/GNA11/CYSLTR2* mutations [9]. The overexpression of *PLCB4* suggests a potential contribution to the activation of Gαq pathway in the absence of *PLCB4* activating mutations. RASGRP3 has been shown to mediate MAPK pathway activation in UM [10], [11]. We identified an additional GPCR downstream pathway gene, *RAPGEF4*, as significantly upregulated in both UM PDX as compared to NM.
Ranking the consistently regulated genes by Log2FC indicated that the top 50 most upregulated genes in MP41 and MP46 are quite similar (Table 1 A and B) as illustrated in gene names in bold. Several non-coding RNAs including HAGLR and TRPM2-AS, which have been previously reported to participate in oncogenesis [12]–[16], were found upregulated in our

comparisons. As several genes from the top 50-upregulated genes are known to play roles in oncogenesis, our analysis may reveal new targets for UM in the set of regulated genes. Concerning down regulated genes in UM vs NM, there is less overlap among the most strongly differentially expressed (Table 1 C and D). Only eight of the top 50 most down regulated genes are shared between models. Consistent with the IHC result, *BAP1* is the most down regulated gene in the MP46 vs NM comparison.

We explored the genomic localization of differentially expressed genes and identified 101 cytobands significantly associated with regulated genes (Supplementary Figure 1A). Among them, the 8q cytobands were the most abundant (18%). Up-regulated genes are significantly associated with cytobands gained in MP41 and MP46 as from chromosomes 8q, 1q, 21q, but also from cytobands from 5q and 4q, which have normal copy number (CN) in MP41 and MP46, or from cytobands from 2p/2q and 7q gained only in MP46. Down-regulated genes are associated with cytobands lost in MP41 and MP46 as from 1p, 3p, 8p 16q, or from 9q, 10q, 19p/q lost only in MP41, from 12q gained only in MP41, and from 17q gained only in MP46.

We next used Reactome analysis to identify enriched pathways in the differentially expressed genes. The top 50 deregulated pathways are shown in Figure 2E. These pathways include proliferation-related pathways (cell cycle, mitosis, checkpoints) as well as chromatin maintenance and DNA repair pathways (DNA double strand break repair, Fanconi anemia) (p-value $<1.5x10^{-4}$, as shown in Supplementary Figures 2-3). DNA damage and repair (DDR) pathways were found to be up-regulated in our comparison. The Homologous Recombination (HR, Supplementary Figure 2B) pathway is the most significantly differentially expressed pathway (p-value: $5.99x10^{-9}$) related to DDR. Upregulation of DNA damage sensors including *MRE11, RAD50*, and *NBN/NBS1* genes are observed in our comparisons, as well as *BARD1, BRCA1/2, BRIP1, PALB2, SEM1, BRCC3, USP3*, several *Rad51* paralogs and *RAD54B*. The Fanconi Anemia (FA, Supplementary Figure 2C) pathway is consistently differentially expressed in UM vs NM comparison with 13 upregulated genes (min pvalue: $2.94x10^{-4}$).

In summary, this analysis revealed a first list of regulated genes (3066 down and 2334 up-regulated genes) in two UM models compared to NMs. Even if significant enrichment is observed on specific cytobands, this list highlights for example the activation of RAPGEF4 and PLCB4 in a context of GNA11/GNAQ mutated UM models. Interestingly sensors of DNA damage repair pathway are activated. In this context *PRAME* upregulation, known as a marker of aggressiveness in UM, was importantly identified as upregulated in MP41 and MP46.

Optical mapping and FISH analyses reveal major chromosomal aberrations in the UM models.

Given the enrichment for increased expression of DDR genes, a structural DNA analysis by optical mapping (Bionano platform [27]) as well as telomere and centromere staining followed by M-FISH (TC+M-FISH [17]) was conducted on MP41 and MP46. Due to technical limitations, we took advantage of cell lines derived from MP41 and MP46 PDXs to achieve DNA optical mapping and M-FISH. The Bionano optical mapping achieved 500bp resolution and a minimum coverage of 97X per sample, which revealed long-range DNA alterations including translocations, insertions, duplications, and small deletions in MP41 and MP46 models (Figure 3 A, B and C). MP41 optical mapping revealed intra-chromosomal translocation as well as inter-chromosomal translocations (t(19;19), t(1;12) or t(6;8)). Long-range alterations were identified in MP46 both inter-chromosomal (i.e. t(1;22)) as well as intra-chromosomal in chr19. Structural variants including deletions, insertions, and duplications were also identified and summarized in Figure 3C.

TC+M-FISH revealed a complex MP41 karyotype (Figure 3D): a hyper-triploid genome with dicentric chromosomes dic(1;11;6;8), dic(1;11), dic(6;8;14) and dic(6;8;17) due to telomeric losses (dic(14;16), i(8q), dic(1;11;8)), and interstitial telomeric sequences: dic(6;8;17) (Supplementary Figure 4). Such chromosome end-to-end fusions are often associated with dicentric chromosomes and aberrant chromosomal structures. MP46 also displays a complex karyotype (Figure 3E): a hyper-diploid genome with multiple dicentric chromosomes: dic(1;17), dic(6;10), dic(8;21) and dic(13;22), dic(16;20); dic(20;22). Two translocations were also identified in MP46: t(1;22) and der(15)t(11;15). In addition to chromosome structural alterations, ring chromosomes were detected in several metaphases, concerning chromosomes 9 and 21 in MP46, and chromosomes 1, 8, and 11 in MP41.

Extending the RNAseq based gene expression analysis, RNA fusion analysis was conducted using multiple algorithms. PCR and Sanger sequencing were carried out to confirm the presence of junctions of fusion RNAs present in MP41 and in MP46. In most cases, structural variants were directly associated to the presence of new fusion RNAs. For example, an insertion-duplication in 12q24 was observed in the Bionano analysis, in MP41 and in MP46, leading to a fusion gene, as *MAPKAPK5-ACAD10* in MP41 and *KDM2B-RHOF* in MP46. This event occurs in the replication fragile site FRA12E [17]. The presence of fusion transcripts *MAPKAPK5-ACAD10* and *KDM2B-RHOF* was confirmed in the respective UM models where the SV occurred. A translocation t(1;22) event was also observed in MP46, leading to the fusion gene *CABIN1-MPRS21*, and a fusion RNAs.

Interestingly, the translocation t(6;8) identified in MP41 is associated with a complex DNA topology, resulting in two new fusion RNAs (*GPAT4-NCOA7* and *POMK-RSPO3*). A FISH analysis using specific probes revealed that a fusion element composed of chr 6 and chr 8 was present on derivative chromosomes 6: der(6)t(6;8); dic(der(6)t(6;8);14); dic(der(6)t(6;8);16); dic(der(6)t(6;8);17), and present on derivative chromosomes 8: der(8)t(6;8), ider(8)(q10)t(6;8)x2, dic(1;11;8;6)x2, and a ring chromosome r(dic1;11;8;6). A specific FISH was carried out on the MP41 cell line targeting: *NCOA7*, *RSPO3* (both on chromosome 6), as well as *GPAT4*, and *POMK* (both on chromosome 8) (Supplementary Figure 5A), combined with a sequential FISH analysis. Normal chromosome 6 were labelled only with *NCOA7* and *RSPO3* probes (Supplementary Figure 5B), contrary to dicentric chromosome 6 which were labelled with all four probes (Supplementary Figure 5C and D). Surprisingly chromosome 8 were labelled by its two genes *GPAT4* and *POMK* as well as *NCOA7* but not with *RSPO3 (*Supplementary Figure 5E). Isochromosome 8 were only labelled with *GPAT4* and *NCOA7*, as dic(1;11;8;6) (Supplementary Figure 5E and F). Such a chromoplexy-like pattern involving regions of chr6 and chr8, originating from chr6/8 centromeres may result from genome instability (Supplementary Figure 5G). Among fusion RNAs, a subset were predicted to code for new fusion proteins. Knowing that *MAPKAPK5-ACAD10* was previously identified as a likely germline variant [18], this fusion may not be useful for further analysis on its oncogenic functions.

To test similar genomic features, additional aggressive uveal melanoma models sharing a 8q gain including OMM1, OMM2.3, Mel202, MM66, MM224, MM309 were analyzed with optical mapping and FISH approaches. Major structural variants were detected in all six UM models. TC+M-FISH was achieved on Mel202, MM66, OMM1 and OMM2.3 cell lines confirming the presence of dicentric chromosomes, marker of chromosomal instability, and telomere instability. Telomere aberrations were present in 7 UM cell lines (MP41, MP46, MEL202, MM66, OMM1 and OMM2.3 [19], [20]) as opposed to normal controls. Translocations and dicentric chromosomes were detected in MEL202 cells: der(6)t(6;17), der(11)t(11;12), der(20)t(8;20); MM66: der(6)t(6;20) ; der(20)t(17;20); der(16)t(12;16); OMM1: der(1)t(1;6) ; der(3)t(2;3) ; der(2)t(2;5) der(4)t(4;17) ; der(6)t(6;8) ; der(16)t(16;17) ; der(16)t(16;21); OMM2.3: der(1)t(1;20) ; der(4)t(1;4) ; der(7)t(7;17) ; der(11)t(10;11) ; dic(5;11,22) ;

der(13)t(10,13) ; der(17)t(6;17) dic(17;19). Those derivative chromosomes were also associated with complex structural variants identified with optical mapping. Although gene expression analysis was not performed for Mel202, MM66, OMM1 and OMM2.3 samples in this work, a recurrent pattern of genomic instability was observed on those 8q gain UM models.

To summarize, high resolution DNA optical mapping combined with TC+M-FISH revealed telomere instability and the presence of numerous, various and complex DNA structural variant in MP41 and MP46, observed in other aggressive UM models.

DNA methylation analysis reveals differences in CpG island (CGI) patterns and identifies BAP1 promoter deletion.

In order to address epigenetic regulation, NM and UM models were analyzed through OxBS sequencing pipeline (Cambridge Epigenetics). This modification of bisulfite sequencing was found to be more robust in our samples, particularly for the normal melanocytes, most probably due to the abundance of melanin.

First, a random forest analysis allowed classification of MP41 and MP46 in the TCGA methylation group 2 (corresponding to BAP1 proficient) and group 4 (BAP1 deficient) respectively.

We next compared the methylation status of UM samples and NM according to genomic localization: CGI promoters, non-CGI promoters, exons, introns, intergenic regions and repeat elements (RepeatMasker annotations). As illustrated in Figure 4A, whereas CGI-promoters are generally equally demethylated in UM samples and NM, tumor samples are globally less methylated in non-CGI promoters as compared to normal samples. Exon, intron and intergenic CGI methylation is also similarly reduced in both MP41 and MP46 compared to normal samples. The same was observed in the methylation profiles of repeat elements, which was found globally lower in UM models. In summary, independent of localization, CGI are less methylated in both of our models of aggressive UM than NM [21], [22].

Next based on CpGs defined in NM, MP41 and MP46, we identified differentially methylated regions (DMR, Figure 4B). About 4 million hypo-methylated DMRs and 1.3 million hyper-methylated DMRs are present in MP41 vs NM. Similar numbers were identified in MP46 with 4.6 million hypo-methylated DMRs and 1 million hyper-methylated DMRs. Importantly, comparisons of hypo and hyper-methylated regions showed that almost half of DMRs are shared by MP41 and MP46 independently of their localization (Figure 4B).

As mentioned before, MP46 clusters with the DNA methylation group 4 of TCGA [6] which includes BAP1-deficient and monosomy 3 UM tumors. As no *BAP1* mutation was previously identified in MP46 [5] despite the absence of BAP1 protein, we analyzed the status of *BAP1* promoter methylation. As shown on Figure 4C, whereas MP41 displays a hypo-methylated promoter with a pattern comparable to that observed in NM (see RNA data in Supplementary Figure 6 A), MP46 has a specific pattern of hyper-methylation in the promoter, especially at the boundaries of a 809bp deletion identified in the whole genome OxBS data, within the referenced CpG129 in UCSC genome browser (hg19; chr3:52,443,678-52,445,104) (Figure. 4C). The *BAP1* promoter is a bidirectional promoter [23] shared by *BAP1* and *PHF7* arranged divergently head to head. The MP46 *BAP1* promoter is deleted and deletion boundaries are hyper-methylated. Furthermore, both *BAP1* and *PHF7* are unexpressed in MP46 (Supplementary Figure. 6 A and B). Despite optical mapping limitations for deletion detection, the *BAP1* promoter deletion was also observed in MP46 with a suitable accuracy respect to DNA labelling (754bp vs 809bp deletion)

This deletion in *BAP1* promoter has not been described in the 1346 ClinVar records and in the Cosmic database. This deletion may explain BAP1 deficiency of MP46 as shown by immunohistochemistry. A targeted NGS approach based on amplicon-sequencing covering *BAP1* using tilling amplicon sequencing (Supplementary Figure 6C) was performed on 53 tumor samples. We identified two additional cases with a similar deletion in the *BAP1* promoter (Supplementary Figure 6D), for which immunohistochemistry confirmed the absence of BAP1 expression (Supplementary Figure 6E). A recent UM case has been internally identified harboring a deletion of *BAP1/PHF7* promoter, wider than that observed in MP46 (2.2kb). In the tumor, BAP1 could not be detected by IHC and the promoter deletion was confirmed by long range PCR (Supplementary Figure 7). This UM case was analyzed in the frame of the French initiative France Medecine Genomique 2025 and thanks to the SeqOIA platform (https://pfmg2025.aviesan.fr/en/)

Next, we proceeded to integrate the gene expression and methylation profiles. First, we analyzed the methylation status of the consistently regulated genes between MP41 and MP46 versus NM. Most of the regulated genes do not a have a significant methylation switch with only 5% of regulated genes displaying a hypo or hyper-methylation of their promoters. Interestingly, some of the most differentially expressed genes, such as *RASGRP3* and *PRAME* discussed above, are part of the minority that do show differential promoter methylation. Importantly, *BAP1* deletion in MP46 was found associated with hypermethylation at deletion boundaries resulting in *BAP1* loss of expression at RNA and protein levels.

DNA topology analysis reveals stable compartments and TADs containing most regulated genes.

To elucidate if regulation of gene expression could be linked to chromatin organization and DNA folding, chromatin structure and DNA topology were investigated. The spatial organization of melanocyte genomes and in particular physical interactions may contribute to the regulation of gene expression during transformation of uveal melanocytes. As DNA, folding may be considered at several levels, a compartment analysis was conducted at 0.25Mb resolution corresponding to open-closed chromatin domains in which the A and B compartments detected by Hi-C reflect the folding of chromosomes into euchromatin and heterochromatin, respectively. The alterations of copy number identified in MP41 and MP46 UM genomes (Supplementary Figure 8) can alter HiC interaction scores [24] (Supplementary Figure 9A, E and I, Supplementary Figure 10 A, E and I), and normalization is necessary to accurately decipher DNA topology. Multiple computational methods for HiC normalization were carried out (ICE, CAIC, and LOIC) on UM models and NM (Supplementary Figure 9 and 10) as performed previously on breast cancer cell lines [25].

Only the CAIC method resulted in a stable distribution of contacts independent of the copy number status, whatever the compartment status is (Supplementary Figure 10C and 10G). Thus, the CAIC normalization allows the analysis of the organization on compartments A/B independently from copy number status.

On the basis of CAIC normalized HiC data, we next compared A and B compartments defined in NM and UM models and identified that most compartments (~72%) share the same status: both A compartments (labelled as ”AAA”, 34.04%) and B compartments (BBB: 37.72%) are stable (Figure 5B). Approximatively 10% of A compartments were shared by NM and only one UM model (4.9% of compartment A shared by NM and MP41 (AAB), 5.94% compartment A shared by NM and MP46 (ABA)); 10% of compartment B were also shared by NM and a UM model (4.19% of compartment B shared by NM and MP41 (BBA), 5.21% compartment B shared by NM and MP46 (BAB)). Changes in compartment status concern 4.36% of

compartment A becoming inactive in both UM models (ABB), and 3.64% of compartment B becoming active in both UM models (BAA). A karyotype view was used to illustrate the position of compartment assignment changes in NM and UM models (Figure 5D).

Next, genes in A/B compartments were examined in our 3 models (NM, MP41, MP46) according with their expression status and regulation in order to depict the regulated genes per type of compartment. Enrichment of differentially expressed genes by compartment status was next analyzed (Figure 5C). As the A compartment (euchromatin) has higher gene content, NM - MP41 - MP46 A compartments (AAA) contain most of the regulated genes. This enrichment is significant with respect to the total of number of regulated genes, number of genes regulated per regulated compartment (AAA, AAB, ABA, ABB, BAA, BAB, BBA, and BBB) (Fisher exact test: 3.21 10^{-07}). Next, the other significantly regulated genes are present in ABA and BBA compartment. The ABB and BAA compartment contain 233 regulated genes, but this is not significant (Fisher exact test: $1.43x10^{-1}$ and $3.25x10^{-1}$, Supplementary Table 4).

Topological associated domains (TADs) were further analyzed in both models. No significant differences were observed in UM and NM, in terms of either number or length of TADs (Figure 5E, 5F). The median size of the TADs based on Hi-C 40kb iced normalization is 1 Mb in NM and both UM models.

Based on this compartment analysis, active to inactive TAD status was compared to differential gene expression. From the differential gene expression analysis, 5400 genes were identified consistently regulated in MP41 and MP46 vs NM with 3,066 down regulated and 2,334 up regulated genes (absolute fold change >1.5, pvalue <0.05). As A compartments are enriched in genes, 9204 genes composed the NM, MP41 and MP46 shared compartments AAA, out of which 2396 are co-regulated in MP41 and MP46 vs NM, meaning that half of regulated genes remain in a stable activated compartments (48.7% of regulated genes). On the other hand, B compartments shared by our 3 models have 3240 genes, out of which 330 are co-regulated in our UM models and corresponding to 6.71% of regulated genes (Figure 2B). In this context, less than 7% of regulated genes are part of condense chromatin (B compartments).

In summary, 83% of regulated genes remains in stable compartments as shown in Figure 4C (AAA BBB, No compartment assigned and Multi compartment assigned containing respectively 48.7%, 6.7%, 22.4% and 5.5% of regulated genes in MP41 MP46 vs NM). More interestingly, 147 regulated genes (~3%) are associated with changes in the compartment status: 58 regulated genes belong to active compartments in MP41 and MP46, and 89 regulated genes belong to inactive compartments. Concerning the remaining regulated genes (674/4921; ~14%), 10% of regulated genes belong to compartments that become inactive in MP41 or MP46, and 4% of regulated genes belong to compartments that become active in MP41 or MP46.

Chromatin topology and histone marks changes are associated with up-regulation of *PRAME*.

To enrich our understanding of chromatin organization and gene expression regulation, chromatin immunoprecipitation and sequencing analysis were carried out on activate epigenetic mark as H3K4me3, and repressive marks H2AUb and H3K27me3, on NM, MP41, and MP46. Additional analyses were achieved on MP41 and MP46 cells, on H3K27Ac and CTCF. As H3K27Ac is recruited on enhancers to activate transcription, and as CTCF is associated to different functions in DNA looping with the cohesin complex, acting as enhancer-

promoter interaction in DNA folding, or as a transcriptional repressor by formation extruding loops, those two marks were analyzed in addition to H3K27me3, H3K4me3, H2Aub, DNA methylation and DNA compartments.

As depicted in Figure 5D, 371 activate compartments were identified specifically in tumor setting (BAA) containing 58 consistently regulated genes (26 consistently down regulated and 37 consistently upregulated) in MP41 and MP46 versus NM. Among the 37-upregulated genes in activated compartments, *PRAME* and *ZNF280A* were found enriched in H3K4me3, 33 genes (including *PRAME, ZNF280A/B, EZH2*) display H3K27Ac peaks, 2 genes lost H3K27me3 marks (*PITX2* and *COL4A5*) and 4 were demethylated in their promoter. Among the 26 downregulated genes, none were enriched in H3K27me3 marks in both UM models, only one gene (*ZC4H2*) lost H3K4me3, 20 genes contain H3K27Ac marks, and no gene displays a hyper methylated promoter.

Upregulated genes associated with activated compartments include *EZH2*, *EPHA4*, and *PRAME*. Among the major regulated genes, PRAME is associated with a particularly high fold change (log2 Fold Change ~12.1 in MP41 and 11.9 in MP46 vs NM). *PRAME* upregulation was identified through two RNAseq analytical approaches: a standard differential gene expression analysis combining RNAseq (Easana, Figure 6A) and a k-mer differential gene expression analysis. Although an absence of *PRAME* expression is observed in our NM, a huge number of *PRAME* counts are present in MP41 and MP46.

The *PRAME* gene is situated on 22q11.22 (hg19 chr22:22,890,123-22,900,022) between tandem Zinc finger proteins *ZNF280A* and *ZNF280B* previously identified as Suppressor of Hairy Wing genes (*SUHW1/ZNF280A* and *SUHW2/ZNF280B*) downstream of *PRAME* and a gene encoding a putative membrane glycoprotein (*POM121L1*) upstream of *PRAME* as illustrated on Figure 6D. In this locus, only *ZNF280A*, *ZNF280B* and *PRAME* are upregulated in a compartment being activated in our UM models compared to NM (Figure 6A). We also observed hyper methylation of the *PRAME* promoter in normal melanocytes and an hypo-methylation in MP41 and MP46 tumor models (Figure 6B), which correlates with the activation of *PRAME* expression in UM (Figure 6A and 6D) [26]. The *PRAME* promoter methylation status has previously been described in UM as a marker of aggressiveness [27].

Concerning histone marks, our analysis revealed at the *PRAME* locus in MP41 and MP46, the presence of active transcription histone marks (H3K4me3, H3K27Ac), and the absence of repressed transcription histone marks such as H3K27me3. In MP46 an additional H3K27Ac is observed in *ZNF280A*, which potentially also leads to the further upregulation of *ZNF280A* expression compared to MP41. In NM, H3K4me3 and H3K27me3 peaks were not observed on the *PRAME* promoter (Figure 6D).

DNA topology analysis at the *PRAME* locus reveals a different pattern in NM compared to UM MP41 and MP46 models. In both tumor models, the DNA topology analysis reveals tight contacts forming an anti- diagonal pattern on the contact map at the *PRAME* locus (Figure 6C). Such tight contacts could be caused by a hairpin structure of a single DNA loop.

Analyzing the ENCODE resource of transcription factor ChIP-seq experiments, 128 transcription factor recognition sites were identified between *ZNF280A/B* and *PRAME* corresponding to 85 different DNA binding factors involved in chromatin and transcription regulation. Among these, 20 are also significantly upregulated in our gene expression analysis (Supplementary Figure 11A). Expressed and upregulated *PRAME* DNA binding factors include cohesion components *RAD21* and *SMC3*, which may contribute to this hairpin like topology. Chromatin organization modifiers such as DNA binding helicases *CHD1* and *CHD2*, were also found upregulated in our analysis. All of these proteins are associated with chromatin remodeling and may contribute to PRAME overexpression in our UM models.

Due to cohesin subunit RAD21 multiple functions in DNA repair, sister chromatid segregation, biogenesis of centrosomes, chromatin organization, and transcription regulation[28]–[30], and because of RAD21 copy number gain (8q+) and upregulation in our UM models, *RAD21* depletion was carried out using siRNA (Supplementary Figure 11C) to evaluate its potential role in *PRAME* regulation in a cell line derived from MP41. *RAD21* downregulation was confirmed at both RNA and protein levels and resulted in a significant decrease of cell viability as expected (34% respect to control, Supplementary Figure 11D, [31]) but *PRAME* gene expression did not change after 72h. While these results may indicate that *RAD21* is not necessary for the activation of *PRAME* expression, depleting Cohesin components has drastic effects on replication and limit the time frame which can be assayed (Supplementary Figure 9D).

Overall, we have identified a novel mechanism of PRAME gene expression dysregulation.

Discussion

In this study we report for the first time a multi-omics approach comparing pure melanoma populations obtained from two aggressive UM models with short-term cultured normal choroidal melanocytes. The multi-omics analysis includes whole genome somatic mutations, transcriptome, copy number, methylome, DNA optical mapping, FISH, histone modifications, and DNA topology analysis by HiC. In order to obtain a sufficient number of pure melanoma cells we performed cell sorting on two PDXs generated from aggressive UM primary tumors. The tumor sample MP41 does not display any identifiable BSE event, expresses BAP1 and is classified in the TCGA group enriched in SF3B1-mut UM. The second tumor sample, MP46, belongs to the TCGA high-risk group and does not express BAP1 despite the absence of mutations in the BAP1 coding sequence. These two samples were compared to NM obtained by maintaining choroidal membranes in culture from healthy donors

Although disomy 3 UM patients display a favorable outcome some of them develop metastases. This is the case of the patient from whom MP41 was derived. Interestingly in the TCGA cohort a third of disomy 3 UM samples (13 out of 38) does not display a BSE event whereas the absence of BSE event is rare in the monosomy samples (3 out of 42). Given the absence of a BSE mutational event in MP41 we carefully looked at the whole genome sequencing data to try to identify mutations explaining tumor progression in MP41. In addition to *GNA11* mutation, a nonsense truncating mutation in *KMT2C* was predicted as an oncogenic driver. This gene is altered in about 5% of cancers but *KMT2C* mutations have not been described in UM [32]. Interestingly *KMT2C* inactivation has been shown to promote colorectal cancer development through enhancer H3K4me1 changes and transcriptional dysregulation affecting a number of pathways with known cancer relevance [33]. Given that some KMT2C functions are not dependent on the integrity of the catalytic domain [34] the contribution of enzymatic-independent activity of KMT2C in cancer development cannot be excluded. The RNA level of *KMT2C* in MP41 is not significantly different of that displayed by NM and we observed a very high expression of this gene in MP46 (data not shown). Further functional studies restoring the wild-type allele of KMT2C in cell lines derived from MP41 need to be performed to explore the potential contribution of the nonsense KMT2C mutation in UM. The aggressivity of MP41 remains elusive in the absence of a BSE event and alterations other than mutations can probably explain this aggressive behavior.

We provide gene expression profiling data of particular interest for the UM scientific community. The list of deregulated genes can help to identify new players in UM oncogenesis and potential new therapeutic targets. Interestingly, *PLCB4* and *RASGRP3* were among the top 50 upregulated genes in tumor samples. Whereas activating mutations of *PLCB4* have been described in UM, our data suggests that high *PLCB4* gene expression can also contribute to over-activation of the PKC pathway in combination with mutually exclusive activating mutations of *GNAQ/GNA11/CYSLTR2/PLCB4*. The overexpression of *RASGRP3* in UM samples is also of particular interest given that this protein has been shown to mediate MAPK pathway activation in UM [10], [11]. In the current study we have identified an additional GPCR downstream pathway gene, the Rap guanine nucleotide exchange factor *RAPGEF4* which is significantly upregulated in both UM PDX as compared to NM. Further functional studies must be conducted to evaluate the potential role of this protein in UM

UM is considered to display a relatively simple pattern of karyotypic alterations in comparison with other solid tumors. This can suggest that UM is a cancer with low generalized chromosomal instability as compared to other cancers. Interestingly DNA repair is among the most deregulated pathways using Reactome analysis of our gene expression profiling data when tumor and healthy melanocytes were compared. The TCGA consortium has described an activation of DNA damage repair in transcription-based cluster 4, which correlates with UM samples from patients with the poorest prognosis. Our structural DNA analysis conducted on MP41 and MP46 combining optical mapping and FISH analysis revealed multiple chromosome aberrations including intra and inter chromosomal translocations, insertion-duplications, telomeres shortening and telomere aberrations. These telomeres and chromosomal aberrations suggest a genomic instability, consistent with the observed deregulated expression of the DNA repair machinery. Importantly we observed chromosomal aberrations by optical mapping and FISH approaches in six other UM cell lines strongly suggesting that genomic / chromosomal instability is a hallmark of UM.

Bi-allelic inactivation of *BAP1* is associated with an increased risk of metastasis in patients with uveal melanoma. Detection of BAP1 deficiency is therefore important to guide UM patient care. Similar to many tumor suppressors, the large diversity of *BAP1* mutations makes difficult the accurate detection of BAP1 gene alterations. In this work, we describe a novel genomic source of BAP1 deficiency consisting of a deletion on the *BAP1* promoter and boundary hyper methylation. A targeted NGS approach identified two other cases of UM displaying deletion in the same genomic area resulting in the lack of BAP1 expression indicating a degree of recurrence of this event. Given the correlation of BAP1 deficiency with the risk of developing metastases our results indicate that in UM patients it will be necessary to look at the BAP1 promoter when mutations or indels in the coding sequence are not detected. This has been recently implemented in Institut Curie where UMs are subjected to NGS in the context of the National initiative “France Medecine Genomique 2025” and we have recently detected an additional UM case displaying the deletion of the *BAP1* promoter.

DNA topology was investigated by using an in situ HiC approach. To reduce bias in the HiC contact matrix due to copy number variations, we benchmarked several computational approaches to normalize the HiC data at the whole genome scale and get exploitable data on compartments and TADs. Most changes in gene expression between NM and our two UM models were not accompanied with changes in compartment status. Compared to the number of differentially expressed genes, relatively few compartments were systematically activated or repressed in UM models versus NM. An important exception to this general pattern could be observed at the *PRAME* locus, where striking differential expression is accompanied by compartment switching and a qualitative change in the intra-TAD contact pattern. This again highlights the insights that a multi-omics approach can offer as chromatin confirmation alterations are not readily identifiable by standard approaches. Further investigation of

repositioned compartments identified in our comparison could help address questions of compartment specificity recently identified in other tumor types [35].

Many cancer testis antigens were significantly enriched among the consistently upregulated genes in tumor versus normal samples. Among these *PRAME* was the highest cancer testis antigen expressed by both MP41 and MP46. *PRAME* has previously been identified as a biomarker for metastatic risk in uveal melanoma [8]. Interestingly, *PRAME* has been shown to be aberrantly hypomethylated and its subsequent activation was found in both class 1 and class 2 uveal melanomas [27]. Consistent with those results, we observed hypo-methylation in MP41 and MP46 tumor models as compared to NM. We further mapped the presence of activate histone marks (H3K4me3, H3K27Ac), and the absence of repressed transcription histone marks such as H3K27me3 in the tumor samples. The activate histone marks were absent in NM (Figure 5D). Importantly, we have observed a different DNA topology pattern between tumor and normal melanocytes by HiC analysis at the PRAME locus. A tumor-specific anti-diagonal pattern found at this locus (Figure 3C) suggests the potential presence of a hairpin structure of a single loop structure with contacts aligned from base to midpoint.

The *PRAME* gene is situated on 22q11.22 between tandem Zinc finger proteins *ZNF280A* and *ZNF280B*. Using the ENCODE resource of transcription factor ChIP-seq experiments we could identify in this genomic space 128 transcription factor recognition sites corresponding to 85 different DNA binding factors involved in chromatin and transcription regulation. Gene expression analyses detected the upregulation of 20 DNA binding factors in tumor samples as compared to normal melanocytes (Supplementary Figure 11A). Importantly among these factors we found cohesin components *RAD21* and *SMC3*, which may contribute to the hairpin like topology observed by HiC. Chromatin organization modifiers such as DNA binding helicases *CHD1* and *CHD2*, were also found upregulated in our analysis. All of these proteins are associated with chromatin remodeling and may contribute to PRAME overexpression in our UM models. We specifically explored whether RAD21 plays a role in the activation of *PRAME* gene expression by depletion of *RAD21* by siRNA. Although our data suggest that RAD21 overexpression may not be necessary for the activation of PRAME expression it is important to note that depleting cohesion components results in drastic effects on replication and limits the time frame to perform functional assays (Supplementary Figure 11E). Further experiments are necessary to evaluate the contribution of the different DNA binding factors identified in this work on the DNA topology changes resulting in the overexpression of PRAME

In summary, our study illustrates how multi-omics integrative approaches conducted in a limited number of samples can improve the understanding of tumorigenesis and reveals two novel mechanisms of gene expression dysregulation in UM with potential clinical implications.

Methods

Isolation of UM cells from PDX.

As described before [3], [4], [36], MP41 and MP46 xenograft tumors were harvested before they reached a volume of 1 cm3 following ethical rules, and processed immediately for dissociation, immunolabelling and sorting based on Petit et al protocol[37]. To avoid isolation of heterogeneous UM cell populations in batches of experiments, immunostaining was conducted with the anti Muc18 containing a rabbit Fc: clone 8H2rFc, also with anti CEACAM1 (8G5hFc) and anti NG2 (14A7hFc) as characterized previously [36]. Secondary antibodies were anti rabbit FC-AF647nm to reveal Muc18 labelling, and anti-human Fc to reveal at the same time CEACAM1 and NG2 labelling. Cell sortings were conducted with the help of

cytometry platforms of Institut Curie on single live cells. In total, 15-20 mice were grafted per model, generating 225*.10^6 cells for MP41 and 133*.10^6 cells for MP46. Twelves batches of dissociation and cell sorting were carried out for MP41 and 10 batches for MP46 generating in total 225.10^6 and 133.10^6 cells respectively for MP41 and MP46. After each cell sorting, a fraction of cells was kept for DNA and RNA extraction, and most cells were fixed according Rao et al protocol.

Normal uveal melanocytes from two healthy donors and 3 preparations obtained after enucleations were dissociated and maintained in culture from choroidal membranes from Pr Simon Saule's lab and Dr Geraldine Liot. After enzymatic (with collagenase) and mechanical dissociation, primary cells were cultured in HAM/F12 supplemented with 10% FBS, Penicillin 100 U/mL, Streptomycin 100 U/mL, 2mM L-glutamine, 2.5µg/mL Amphotericin B. Extemporaneously completed media was supplemented with 0.1mM IBMX, 10ng/µL of Cholera toxin (10 ng/ml final), and 10mg/mL βFGF and filter with a 0.22µm filter. Cell were maintained in a humidified atmosphere with 5% CO2 at 37°C , and culture medium was exchanged twice a week.

Quality control of isolated cells.

To monitor each fraction of MP41/MP46 isolated cells, DNA and RNA were extracted as described before, and tested for chromosomal copy number alterations and gene expression using Affymetrix microarrays respect to previous analysis done on primary tumor or pdx samples [36].
Based on this analysis, pools of MP41 cells and MP46 cells were used for whole genome sequencing, RNAseq, DNA methylation, *in situ* HiC, ChIPSeq experiments, and to allow replicates of in situ HiC and ChIPSeq analyses.

Whole genome analysis.

Genomic DNA was extracted using QIAamp DNA Mini kit, and quality controls were achieved using a Nanodrop ND1000 to evaluate DNA purity and Qubit™ dsDNA BR/HS Assays to evaluate double strand DNA concentration. 250ng of gDNA from MP41 and MP46 sorted cells were characterized using Affymetrix/Thermo Cytoscan HD microarrays to monitor copy number and LOH. Next, two micrograms of MP41 and MP46 DNAs were used to prepare paired-end 100bp Illumina libraries for whole genome sequencing. Genomic DNA from healthy surrounding tissue was sequenced according to approval by ethic committee of Institut Curie to filtered germline mutations.
Whole genome sequencing was conducted on genomic DNA extracted from PDX derived UM cells and from normal tissue preserved from enucleation. Illumina short read sequencing was achieved in two-separated runs due to availability of DNAs. The alignment of the sequenced reads to hg19 was performed with Burrows-Wheeler Aligner (BWA-MEM v0.7.10). MuTect2 from the Genome Analysis Toolkit (GATK v3.5) was used in "Tumor with matched normal" mode to call somatic variants. Somatic point mutation analysis of whole genome sequencing revealed 1348 and 1186 single nucleotide variants in MP41 and MP46 respectively representing less than one somatic mutation per Mb (0.42 and 0.37 SNV/Mb) as observed in UM [6]. Detected variants with a frequency in the normal sample greater than 20% were filtered out. Variants in UM models were selected according coverage (>10), read counts (>20) and allele frequency (>20%) in UM models. Cancer Genome Interpreter (CGI, [38]) and VarSome tools (containing 10 pathogenic predictions, [39]) were combined to characterize variants.

Whole genome DNA methylation analysis was carried out with a Cambridge Epigenetics kit (TrueMethyl kit) that corresponds to an oxidative bisulfite reaction, to identify and analyze only 5-methylcytosine (5-mC). Briefly 400ng of genomic DNA were used to first perform an oxidation reaction, that converts 5-hydroxymethylcytosine (5-hmC) to 5- formylcytosine(5fC), thus after a bisulfite conversion, unmodified C and 5FC will be converted into uracils and sequenced as

thymines contrary to 5mC that remains sequence as a cytosine. Libraries were sequenced on an Illumina Hiseq as paired end 100bp. Differentially methylated regions (DMR) were assigned when a methylation difference of 30% occurs at least on 10 CpGs in a minimum of 500bp windows; windows are merged if distant between two DMRs is less than 500bp.

Chromatin structure analysis.

An *in situ* Hi-C method proposed by Rao et al [40] was applied for compartments and Topologically Associating Domains (TAD) analyses. Analysis were conducted in duplicates for 3 NM, 2 UM models (MP41 and MP46) from. After cell sorting of MP41 and MP46, cells were fixed as recommended and stored at -80°c until the recovery and control of cells for all modes in duplicates. Briefly, $3x10^6$ cells fixed in formaldehyde were permeabilized, and an MboI digestion was conducted on cell nuclei. DNA ends were biotinylated at their extremity and next ligated according their proximity. After a decrosslinking step with Proteinase K, DNA was purified according on phenol/chloroform protocol, quantified and sheared to a size of 400-500bp. Next biotinylated DNA was pulled down using Dynabeads MyOne streptavidin T1 beads (Life technologies), and DNA was repaired with a mixture of T4 DNA ligase, T4 DNA polymerase I, DNA polymerase I, large Fragment, and T4 Polynucleotide Kinase. After a purification step, a dA-tail was added to DNAs with a Klenow exo minus, A final purification step was achieved prior to Illumina adaptor ligation. The last steps consisted of a PCR amplification with a selection of 12 cycles using Illumina primers. An equimolar pool of libraries was sequenced on an Ilumina HiSeq - rapid Run generating $250\text{-}436x10^6$ pairs HiC data were processed with HiC-Pro before comparison of 3 different normalization (CAIC, LOIC and ICE methods, [25]).

DNA Optical mapping and cytogenetics analysis.

Structural variant analysis was conducted with Bionano DNA optical mapping from $1.5x10^6$ MP41 and MP46 cell pellets. A direct labelling on CTTAAG motif (DLE1) was conducted according to Bionano recommendations. Labelled DNA were analyzed on a Saphyr system. A De novo assembly was carried out using the Bionano serve 1.6. Molecule N50 was 407.8kbp for MP41, label density was 16.3 per 100kbp and effective coverage of the assembly was 71.9X. For MP46, molecule N50 was 325.6kbp, label density was 16.9/100kbp and effective coverage of assembly was 84.5X.
Telomere and centromere staining followed by M-FISH technique were applied on cytogenetics slides after colcemid (0.1µg/mL) treatment of MP41 and MP46 cells as described previously [41], [42] to identify numerical and structural chromosomal alterations as well as telomere instability. Briefly, UM cells were cultured in T75 in DMEM with 10-20% SVF depending on models (10% SVF: MP41, Mel202, OMM1, OMM2.3; 20%: MP46). Forty-eight hours after passage, medium was supplemented with colcemid (0.1 µg/mL) for a 3h incubation to arrest dividing cells in metaphase. Cells were harvested, washed, suspended in 10mL DMEM with 0.075 M potassium chloride (Merck, Kenilworth, NJ, USA) and incubated for 20 min in a 37°C water bath (hypotonic shock) and fixed as previously described [41]. Next a telomeres and centromeres followed by M-FISH technique (Metasystems probes, Germany) were performed as previously described [43]. The quantification of telomere FISH signal intensity in interphase cells was performed using Metacyte software (MetaSystems, version 3.9.1, Altlussheim, Germany) and TeloScore Software (Cell Environment, Evry, France).
The mean fluorescence intensity (FI) of telomeres was automatically quantified in 10,000 nuclei on each slide. The settings for exposure and gain remained constant between captures. The experiments were performed in triplicate.

Analysis of metaphase spreads allowed detection of telomere abnormalities and chromosomal aberrations using ChromoScore Software (Cell Environment, Evry France) and Isis software (MetaSystems, Altlussheim, Germany). The images of metaphases were captured using automated acquisition module Autocapt software (MetaSystems, version 3.9.1) and a ZEISS

Plan-Apochromat 63x/1.40 oil (Zeiss, Oberkochen, Germany) and CoolCube 1 Digital High Resolution CCD Camera (MetaSystems, Altlussheim, Germany) with constant settings for exposure and gain.
For each UM model, telomere and chromosomal aberrations were analyzed automatically on 100 metaphases. The scored telomere abnormalities were (i) sister telomere loss, likely occurring in G2, and defined as a telomere signal-free end at a single chromatid, (ii) telomere deletion defined as the loss of two telomere signals on the same chromosome arm (likely resulting from the loss of one telomere in G1/S), an aberration considered to represent double strand breaks, leading to activation of DNA damage response. The scored chromosomal aberrations were dicentric chromosomes, centric rings, translocations, insertions and deletions.

Whole transcriptome analysis.

Total RNA was extracted using miRNeasy kits following supplier recommendations, including a DNAse step. Quality controls were achieved using a Nanodrop ND1000 to evaluate RNA purity and concentration, and on automated electrophoresis to monitor RNA integrity (Bioanalyzer RNA 6000 Nano/Pico kits).
PolyA RNASeq was conducted on total RNA (RIN>7), treated with DNAse
An absolute fold change higher than 1.5 and a p-value below to 0.05 were selected as parameters for detecting differentially expressed genes.
Splicing analysis was conducted with 5 different pipelines: deFuse, SOAPfuse, JAFFA, FusionCatcher, TopHat-Fusion. Fusion RNAs were identified present in at least 2 algorithms, and found in at least 2 replicates per model.

Histone Modifications.

ChIPSeq against H2AUb, H3K4me and H3K27me3 were conducted in simplicate in NM, MP41 and MP46 as published in [52]. ChIpSeq against H3K27Ac and CTCF, were conducted in duplicated in MP41 and MP46 to implement multiomics analysis. 5 million cells were fixed according the protocol used for in situ HiC experiments for H2AUb, H3K4me3, and H3K27me3, and for H3K27ac and CTCF. The chromatin was prepared using the iDeal ChIP seq kit from Diagenode for Transcription Factor protocol. Shearing conditions were setup as 10 minutes using the following settings: 10 cycles of 30'' [ON] 30'' [OFF]. The shearing efficiency was monitored after reversion of the crosslinking and purification of the DNA. For increased sensitivity, an automated capillary electrophoresis system Fragment Analyser was used for chromatin shearing assessment (High sensitivity NGS fragment kit). ChIP assays were performed as defined in the optimizations using 10 µg or 1µg of chromatin per IP with the optimal antibody quantity resulting in the higher enrichment and lower background (CTCF 1µg, H3K27ac 1µg) IPs with a negative control isotype (IgG) were performed in parallel. For each sample, a library preparation was performed on ChIP and input DNA using the MicroPLEX v3 protocol. A control library was processed in parallel with the samples using a control Diagenode ChIP DNA. Five cycles of pre-amplification were performed and 1 µl of each library was analyzed by qPCR in order to determine the optimal amplification cycles required to obtain enough DNA for sequencing. Libraries were then loaded on Fragment Analyzer to check if enough material was generated. After the amplification, the libraries have been purified using AMPure beads and eluted in Tris. Then, the purified libraries were quantified using the Qubit ds DNA HS kit and analyzed on the Fragment Analyzer to assess their size. Using the quantification values from the Qubit and the size measurement generated by the Fragment Analyzer, the molar concentration of each library was calculated.

The quality control of the fastq files was performed using FastQC. The sequences were aligned on hg19 assembly using bowtie2. Duplicates were marked and filtered out using Picard tools MarkDuplicates and samtools. The peak calling was performed using macs2 callpeak function. The parameter --broad was used for the Histone samples, not for the transcription factor

samples. The affinity binding scores were obtained using DiffBind package in R, TMM normalization was applied. Peaks found in at least 50% of the samples from the same condition were kept. The peaks were annotated using FAST DB.

Acknowledgements

The authors thanks the members of the Institut Curie animal facility involved in UM projects, the members of the cytometry platform of Institut Curie and Hospital Saint Louis in Paris for their support of UM cell sorting, the members of the recombinant protein and nanobodies platforms of Institut Curie, the Pathex platform of Institut Curie for BAP1 immunochemistry, the biological resources center for providing UM samples for the BAP1 analysis. The author thank the Unit of Somatic Genetic at the hospital of Institut Curie for the analysis done on NM. The authors thank the genomics platform of Institut Curie for assistance in STR profiling, copy number analysis, DNA optical mapping of UM samples (Audrey Rapinat, Matéo Bazire), with the support of the Region Ile France (SESAME 2019 grant). High-throughput sequencing was performed by the ICGex NGS platform of the Institut Curie supported by the grants ANR-10-EQPX-03 (Equipex) and ANR-10-INBS-09-08 (France Génomique Consortium) from the Agence Nationale de la Recherche ("Investissements d'Avenir" program), by the ITMO-Cancer Aviesan (Plan Cancer III), and by the SiRIC-Curie program (SiRIC grant INCa-DGOS-4654). The authors also thank the Bionano Genomics company and the GENTYANE platform in Clermont Ferrand for the first analysis of MP41 and MP46 models using optical mapping.

Data availability

Supplementary table 1 is available upon request. Sequencing data generated in this work will be deposited on a public portal.

Bibliography

[1] M. Rodrigues *et al.*, « Evolutionary Routes in Metastatic Uveal Melanomas Depend on MBD4 Alterations », *Clin Cancer Res*, vol. 25, n° 18, p. 5513-5524, sept. 2019, doi: 10.1158/1078-0432.CCR-19-1215.

[2] B. A. Krantz, N. Dave, K. M. Komatsubara, B. P. Marr, et R. D. Carvajal, « Uveal melanoma: epidemiology, etiology, and treatment of primary disease », *Clin Ophthalmol*, vol. 11, p. 279-289, 2017, doi: 10.2147/OPTH.S89591.

[3] F. Némati *et al.*, « Establishment and characterization of a panel of human uveal melanoma xenografts derived from primary and/or metastatic tumors », *Clin. Cancer Res.*, vol. 16, n° 8, p. 2352-2362, avr. 2010, doi: 10.1158/1078-0432.CCR-09-3066.

[4] C. Laurent *et al.*, « Patient-derived xenografts recapitulate molecular features of human uveal melanomas », *Mol Oncol*, vol. 7, n° 3, p. 625-636, juin 2013, doi: 10.1016/j.molonc.2013.02.004.

[5] N. Amirouchene-Angelozzi *et al.*, « Establishment of novel cell lines recapitulating the genetic landscape of uveal melanoma and preclinical validation of mTOR as a therapeutic target », *Mol Oncol*, vol. 8, n° 8, p. 1508-1520, déc. 2014, doi: 10.1016/j.molonc.2014.06.004.

[6] A. G. Robertson *et al.*, « Integrative Analysis Identifies Four Molecular and Clinical Subsets in Uveal Melanoma », *Cancer Cell*, vol. 32, n° 2, p. 204-220.e15, 14 2017, doi: 10.1016/j.ccell.2017.07.003.

[7] S. Alsafadi *et al.*, « Cancer-associated SF3B1 mutations affect alternative splicing by promoting alternative branchpoint usage », *Nat Commun*, vol. 7, p. 10615, févr. 2016, doi: 10.1038/ncomms10615.

[8] M. G. Field *et al.*, « PRAME as an independent biomarker for metastasis in uveal melanoma », *Clin Cancer Res*, vol. 22, nº 5, p. 1234-1242, mars 2016, doi: 10.1158/1078-0432.CCR-15-2071.
[9] P. Johansson *et al.*, « Deep sequencing of uveal melanoma identifies a recurrent mutation in PLCB4 », *Oncotarget*, vol. 7, nº 4, p. 4624-4631, déc. 2015, doi: 10.18632/oncotarget.6614.
[10] A. R. Moore *et al.*, « GNA11 Q209L Mouse Model Reveals RasGRP3 as an Essential Signaling Node in Uveal Melanoma », *Cell Rep*, vol. 22, nº 9, p. 2455-2468, 27 2018, doi: 10.1016/j.celrep.2018.01.081.
[11] X. Chen *et al.*, « RasGRP3 Mediates MAPK Pathway Activation in GNAQ Mutant Uveal Melanoma », *Cancer Cell*, vol. 31, nº 5, p. 685-696.e6, 08 2017, doi: 10.1016/j.ccell.2017.04.002.
[12] C. Yang *et al.*, « Long noncoding RNA HAGLR acts as a microRNA-143-5p sponge to regulate epithelial-mesenchymal transition and metastatic potential in esophageal cancer by regulating LAMP3 », *The FASEB Journal*, vol. 33, nº 9, p. 10490-10504, 2019, doi: https://doi.org/10.1096/fj.201802543RR.
[13] R. F. Gillespie et L. J. Gudas, « Retinoid Regulated Association of Transcriptional Coregulators and the Polycomb Group Protein SUZ12 with the Retinoic Acid Response Elements of Hoxa1, RARβ2, and Cyp26A1 in F9 Embryonal Carcinoma Cells », *J Mol Biol*, vol. 372, nº 2, p. 298-316, sept. 2007, doi: 10.1016/j.jmb.2007.06.079.
[14] M. Sauvageau *et al.*, « Multiple knockout mouse models reveal lincRNAs are required for life and brain development », *eLife*, vol. 2, déc. 2013, doi: 10.7554/eLife.01749.
[15] U. Orfanelli, A.-K. Wenke, C. Doglioni, V. Russo, A. K. Bosserhoff, et G. Lavorgna, « Identification of novel sense and antisense transcription at the TRPM2 locus in cancer », *Cell Res*, vol. 18, nº 11, p. 1128-1140, nov. 2008, doi: 10.1038/cr.2008.296.
[16] J. Xiao *et al.*, « Long noncoding RNA TRPM2-AS acts as a microRNA sponge of miR-612 to promote gastric cancer progression and radioresistance », *Oncogenesis*, vol. 9, nº 3, mars 2020, doi: 10.1038/s41389-020-0215-2.
[17] R. Kumar, G. Nagpal, V. Kumar, S. S. Usmani, P. Agrawal, et G. P. S. Raghava, « HumCFS: a database of fragile sites in human chromosomes », *BMC Genomics*, vol. 19, nº Suppl 9, p. 985, avr. 2019, doi: 10.1186/s12864-018-5330-5.
[18] R. Holt *et al.*, « CNVs leading to fusion transcripts in individuals with autism spectrum disorder », *Eur J Hum Genet*, vol. 20, nº 11, p. 1141-1147, nov. 2012, doi: 10.1038/ejhg.2012.73.
[19] K. G. Griewank *et al.*, « Genetic and Molecular Characterization of Uveal Melanoma Cell Lines », *Pigment Cell Melanoma Res*, vol. 25, nº 2, p. 182-187, mars 2012, doi: 10.1111/j.1755-148X.2012.00971.x.
[20] M. J. Jager, J. A. B. Magner, B. R. Ksander, et S. R. Dubovy, « Uveal Melanoma Cell Lines: Where do they come from? (An American Ophthalmological Society Thesis) », *Trans Am Ophthalmol Soc*, vol. 114, p. T5, août 2016.
[21] M. A. Gama-Sosa *et al.*, « The 5-methylcytosine content of DNA from human tumors. », *Nucleic Acids Res*, vol. 11, nº 19, p. 6883-6894, oct. 1983.
[22] A. P. Feinberg et B. Vogelstein, « Hypomethylation distinguishes genes of some human cancers from their normal counterparts », *Nature*, vol. 301, nº 5895, p. 89-92, janv. 1983, doi: 10.1038/301089a0.
[23] M. Q. Yang, L. M. Koehly, et L. L. Elnitski, « Comprehensive Annotation of Bidirectional Promoters Identifies Co-Regulation among Breast and Ovarian Cancer Genes », *PLoS Comput Biol*, vol. 3, nº 4, p. e72, avr. 2007, doi: 10.1371/journal.pcbi.0030072.
[24] X. Wang *et al.*, « Genome-wide detection of enhancer-hijacking events from chromatin interaction data in rearranged genomes », *Nat Methods*, vol. 18, nº 6, p. 661-668, juin 2021, doi: 10.1038/s41592-021-01164-w.
[25] N. Servant, N. Varoquaux, E. Heard, E. Barillot, et J.-P. Vert, « Effective normalization for copy number variation in Hi-C data », *BMC Bioinformatics*, vol. 19, sept. 2018, doi: 10.1186/s12859-018-2256-5.

[26] T. Schenk, S. Stengel, S. Goellner, D. Steinbach, et H. P. Saluz, « Hypomethylation of PRAME is responsible for its aberrant overexpression in human malignancies », *Genes, Chromosomes and Cancer*, vol. 46, nº 9, p. 796-804, 2007, doi: https://doi.org/10.1002/gcc.20465.
[27] M. G. Field *et al.*, « Epigenetic reprogramming and aberrant expression of PRAME are associated with increased metastatic risk in Class 1 and Class 2 uveal melanomas », *Oncotarget*, vol. 7, nº 37, p. 59209-59219, juill. 2016, doi: 10.18632/oncotarget.10962.
[28] H. Cheng, N. Zhang, et D. Pati, « Cohesin subunit RAD21: From biology to disease », *Gene*, vol. 758, p. 144966, oct. 2020, doi: 10.1016/j.gene.2020.144966.
[29] J. M. Rhodes, M. McEwan, et J. A. Horsfield, « Gene regulation by cohesin in cancer: is the ring an unexpected party to proliferation? », *Mol Cancer Res*, vol. 9, nº 12, p. 1587-1607, déc. 2011, doi: 10.1158/1541-7786.MCR-11-0382.
[30] R. V. Skibbens, J. Marzillier, et L. Eastman, « Cohesins coordinate gene transcriptions of related function within Saccharomyces cerevisiae », *Cell Cycle*, vol. 9, nº 8, p. 1601-1606, avr. 2010.
[31] H. Xu *et al.*, « Enhanced RAD21 cohesin expression confers poor prognosis and resistance to chemotherapy in high grade luminal, basal and HER2 breast cancers », *Breast Cancer Res*, vol. 13, nº 1, Art. nº 1, févr. 2011, doi: 10.1186/bcr2814.
[32] R. Zhang, H.-X. Wu, M. Xu, et X. Xie, « KMT2A/C mutations function as a potential predictive biomarker for immunotherapy in solid tumors », *Biomark Res*, vol. 8, p. 71, déc. 2020, doi: 10.1186/s40364-020-00241-0.
[33] C. Larsson *et al.*, « Restoration of KMT2C/MLL3 in human colorectal cancer cells reinforces genome-wide H3K4me1 profiles and influences cell growth and gene expression », *Clinical Epigenetics*, vol. 12, nº 1, p. 74, mai 2020, doi: 10.1186/s13148-020-00863-z.
[34] K. M. Dorighi *et al.*, « Mll3 and Mll4 Facilitate Enhancer RNA Synthesis and Transcription from Promoters Independently of H3K4 Monomethylation », *Mol Cell*, vol. 66, nº 4, p. 568-576.e4, mai 2017, doi: 10.1016/j.molcel.2017.04.018.
[35] Y. Liu *et al.*, « Systematic inference and comparison of multi-scale chromatin sub-compartments connects spatial organization to cell phenotypes », *Nat Commun*, vol. 12, nº 1, p. 2439, mai 2021, doi: 10.1038/s41467-021-22666-3.
[36] R. Crépin *et al.*, « Nanobodies against surface biomarkers enable the analysis of tumor genetic heterogeneity in uveal melanoma patient-derived xenografts », *Pigment Cell Melanoma Res*, vol. 30, nº 3, p. 317-327, 2017, doi: 10.1111/pcmr.12577.
[37] V. Petit *et al.*, « Optimization of tumor xenograft dissociation for the profiling of cell surface markers and nutrient transporters », *Lab Invest*, vol. 93, nº 5, p. 611-621, mai 2013, doi: 10.1038/labinvest.2013.44.
[38] D. Tamborero *et al.*, « Cancer Genome Interpreter annotates the biological and clinical relevance of tumor alterations », *Genome Med*, vol. 10, nº 1, p. 25, mars 2018, doi: 10.1186/s13073-018-0531-8.
[39] C. Kopanos *et al.*, « VarSome: the human genomic variant search engine », *Bioinformatics*, vol. 35, nº 11, p. 1978-1980, juin 2019, doi: 10.1093/bioinformatics/bty897.
[40] S. S. P. Rao *et al.*, « A 3D Map of the Human Genome at Kilobase Resolution Reveals Principles of Chromatin Looping », *Cell*, vol. 159, nº 7, p. 1665-1680, déc. 2014, doi: 10.1016/j.cell.2014.11.021.
[41] R. M'kacher *et al.*, « Telomere and Centromere Staining Followed by M-FISH Improves Diagnosis of Chromosomal Instability and Its Clinical Utility », *Genes (Basel)*, vol. 11, nº 5, avr. 2020, doi: 10.3390/genes11050475.
[42] R. M'kacher *et al.*, « The Transition between Telomerase and ALT Mechanisms in Hodgkin Lymphoma and Its Predictive Value in Clinical Outcomes », *Cancers (Basel)*, vol. 10, nº 6, mai 2018, doi: 10.3390/cancers10060169.
[43] R. M'kacher *et al.*, « New tool for biological dosimetry: reevaluation and automation of the gold standard method following telomere and centromere staining », *Mutat Res*, vol. 770, p. 45-53, déc. 2014, doi: 10.1016/j.mrfmmm.2014.09.007.

Legends

Figure 1: Principal characteristics of MP41 and MP46 PDXs established from aggressive uveal melanomas. A. Clinical characteristics of UM cases. B. Main molecular characteristics of corresponding patient derived xenograft models established and characterized previously from Amirouchene-Angelozi et al, 2014. Mutational status were assessed with Sanger sequencing (*GNAQ/GNA11, BAP1, SF3B1, EIF1AX*), with Cytoscan HD microarrays for copy number analysis and BAP1 immunohistochemistry from FFPE tissue section.

Figure 2: Gene expression global overview. A. Principal component analysis of RNASeq of 6 normal choroidal melanocytes (blue), 4 preparations of MP41 UM cells (red) and 3 preparation of MP46 UM cells (green). B. Hierarchical clustering of same samples. C. Differential gene expression analysis of MP41 vs NM and MP46 vs NM to identify genes with a Log2 fold change superior than 1.5 and a p-value lower than 0.05. Up regulated genes (4149 in MP41 vs NM and 4337 in MP46 vs NM) and down regulated genes (4063 in MP41; 5031 in MP46 vs NM) were compared, identifying 2334 commonly upregulated genes and 3066 commonly down regulated genes. D. Heatmap of commonly regulated genes in MP41 and MP46 vs NM. RNA from NM, MP41 and MP46 are represented in blue, red in green respectively. E. 50 most highly regulated pathways by Reactome analysis of commonly regulated genes listed according the significance (-log 2 (p-value +1x10-^{10})).

Figure 3: DNA optical mapping and FISH analysis highlight chromosome aberrations in MP41 and MP46. A and B. Circos plot of MP41 and MP46. From the central to the periphery of the circos plot: whole genome view is summarizes as intra and inter chromosomal translocation (pink lines), copy number gain and losses listed on the first internal layer of the circos, and structural variants as insertion, deletion inversion and duplication are labelled as colored dots on the last results track. Gene density, cytobands and chromosomes are composing the last layers of the circos. C. Number of insertions, deletions, inversions and duplications and inter and inter translocations are detailed for MP41 and MP46 defined by BioNano optical mapping and *De novo* assembly pipeline. D and E. are composed of two different FISH analyses. Upper left picture is corresponding to a telomere (red signal) and centromere (green signal) staining and counter labelled with DAPI (blue). Lower left pictures is from a M-FISH analysis. Main figure correspond to the karyotype view of MP41 (D) and MP46 (E).

Figure 4: Whole genome DNA methylation reveals differences between UM models and normal melanocytes. A. DNA methylation levels based on oxidative bisulfite DNA treatment followed by whole genome sequencing, is shown at CGI promoters, non-CGI promoters, non-promoters CGI, exons, introns, intergenic regions, and on repeats, in normal melanocytes, MP41 and MP46. Percentage of CGI methylation is represented per genomic localization and sample type. B. Differentially Methylated Regions (DMRs) as hypo and hyper DMRs were established in 300kb window in MP41 vs Nm, MP46 vs Nm, and in MP41 vs MP46 comparisons. C. Percentage of CGI methylation in MP41, MP46 and NM in *BAP1* locus through UCSC Genome Browser is represented in yellow. CpG Island 129 overlaps the *BAP1/PHF7* promoter.

Figure 5: Compartments and Topologically Associated Domains (TAD) in normal melanocytes and uveal melanoma models. A. Contacts maps based on in situ HiC seq at the whole genome level for NM, MP41 and MP46. B. Histogram of compartment changes in NM, MP41 and MP46. Compartments identified at a 250kb resolution as A compartment (euchromatin) and B compartments (heterochromatin) and compared for compartment status. 10364 compartments were analyzed and ordered as NM-MP41-MP46, active to inactive compartments: AAA, AAB, ABA, ABB, BAA, BAB, BBA and BBB. C. Integration of compartment changes and gene expression between NM, MP41 and MP46. D. Localization of

inactivated (ABB) and activated (BAA) compartment in MP41, MP46 vs NM on a whole genome view. E and F. Number and size of TADs in NM, MP41 and MP46.

Figure 6: Multiomics analysis revealed a specific *PRAME* activation pattern. A. Gene expression of *PRAME* and its neighbors as *BMS1P20, ZNF280B, ZNF280A* upstream genes and *POM121LP* downstream. FPKM RNAseq data of NM, MP41 and MP46 replicates. B. Percentage of DNA methylation in UCSC Genome Browser (hg19) are represented in golden bars. C. DNA contacts maps of NM, MP41 and MP46 set at 5kb resolution in *PRAME* TAD (blue square). D. *PRAME* integrative view in UCSC Genome Browser, with RefSeq genes, DNA methylation, log2 RNAseq, H2AUb, H3K4me3, H3K27me3, H3K27ac and CTCF peaks.

Supplementary Figure 1: Gene expression regulation in MP41 and MP46. A. Localization of the 2334 upregulated genes and the 3066 down regulated genes are represented respectively in red and green on a chromosome view. A direct comparison of MP41 vs MP46 was conducted and numbers of up/down regulated genes are presented in B and summarized by heatmap (C). Reactome analysis on regulated genes as the top 50 significant regulated pathways (D).

Supplementary Figure 2: From the regulated genes shared in MP41 and MP46 vs NM, main regulated pathways studied in Reactome highlighted by Kegg maps. Gene names are colored depending on their regulation: non-regulated gene are in white boxes, upregulated genes in red boxes and downregulated genes in green boxes. A. Cell cycle pathway (HSA04110, KEGG) contains 124 genes out of which 43 are regulated with 28 up and 15 down regulated, with a min p-value of $5.3x10^{-7}$. B. Homologous recombination (HR) pathway (HSA03440, Kegg) shows 21 out of 41 genes regulated (17 up and 4 downregulated) with a significant value (minimum p-value: $5.99x10^{-9}$). C. Fanconi Anemia pathway (FA, HSA03460, Kegg) is also significantly regulated (min p-value: 2.94x10-4) as 19 out of 54 genes of the pathway are regulated (13 up and 6 down).D. On the opposite to HR, the non-homologous end joining pathway (HHEJ, HAS03450, Kegg) is lowly regulated as 4 out 13 are regulated with a min p-value of $8.22x10^{-2}$ as 3 and 1 genes are respectively up and down regulated.

Supplementary Figure 3: Other Reactome regulated pathways are listed. **A.** P53 signaling pathway is also one of the most regulated pathway including 32 regulated out the 72 genes included in the pathway (14 up and 18 down, min p-value $1.18x10^{-6}$). **B.** Apoptosis pathway (HSA04210, Kegg) contains 52 of 136 regulated genes (20 up and 32 down regulated genes, min p-value $2.47x10^{-7}$).

Supplementary Figure 4: Telomere analysis was monitored on MP41, MP46 and normal fibroblast as controls. A. Telomere labelling intensities were quantified on the 3 models, and distribution of intensity was observed as surface dependent and specific to cell type. B. After a two-step normalization analysis, taking into account size of cells, number of chromosomes per cell and amount of telomere signal per cell, a telomere loss/chromosome average was calculated in MP41, MP46 and fibroblast control (containing respectively an average of 76.8 chromosomes in MP41, 44.8 chromosomes in MP46 and 46 chromosomes per control). Yellow stars highlight telomere loss on 3 chromosomes of MP41. Frequency of telomere loss and deletion per metaphase in MP41 and MP46 cells has been presented, concerning most chromosomes of MP41 and MP46 cells. C. Telomere loss and deletions frequency per chromosome shows specific chromosomes telomere aberrations such as chromosome 6, 8, 14, 17 and 22 in MP41 cells. D Example of telomere defects as interstitial telomere observed on dicentric (6;8;17) in MP41, and on a derivative chr15. Telomere deletion on dic(14;16) , i8q, and chr6, and chr 14q are illustrated.

Supplementary Figure 5: FISH analysis using specific probes reveals the complexity of the rearrangements implicated chromosome 6 and 8 (A) specific probes (Empire Genomic, US) have been designed for the detection of 4 genes: *GPAT4* (green), *POMK* (red), *RSPO3* (blue) and *NCOA7* (orange). (B) the presence of *RSPO3* and *NCOA7* in chromosome 6 without rearrangements (C) dic(6;8;17) showing the presence of *GPAT4* and *POMK* genes in addition to *RSPO3* and NCOA7 in the breakpoint of this aberration. (D) dic(6;8;16) showing the presence of *GPAT4* and *POMK* genes in addition to *RSPO3* and *NCOA7* (E) the i(8q) shows the presence of *GPAT4* and *NCOA7*. (F) dic(1;11;6;8) shows the insertion of the *GPAT4* and *NCOA7* in the breakpoint of this rearrangement (G) possible mechanisms in the formation of these rearrangements implicated chromosome 6 and 8.

Supplementary Figure 6: Identification of *BAP1* deletion leading to *BAP1* loss of expression. A and B. Gene expression detection based on RNAseq analysis (FPKM counts) of *BAP1* and *PHF7* in NM, MP41 and MP46 samples. Absence of *BAP1* and *PHF7* gene expression is observed in MP46 replicates. C. A targeted sequencing based on tilling amplicons (250bp) to characterize *BAP1, SF3B1, EIF1AX, GNAQ* and *GNA11* mutation in a series of 51 UM recently grafted for new UM PDX at Institut Curie. D. Detection of *BAP1/PHF7* promoter deletion in IGV. Blue track corresponds to NM sample, yellow track corresponds to MP41 and orange track corresponds to MP46. Gray track corresponds to new UM cases with a low coverage on *BAP1* promoter associated to a loss of BAP1 protein expression assessed by IHC (E).

Supplementary Figure 7: Example of *BAP1* promoter deletion identified in clinical daily practice. A. Identification of BAP1 promoter deletion (2.2kb) based on exome analysis. B. Validation of the loss of BAP1 expression in nucleus by IHC. C. Confirmation of the deletion of *BAP1* promoter by long range PCR in MP46 and new patient's tumor.

Supplementary Figure 8: Comparison of WGS and HiC copy number profiles for MP41 and MP46. Two whole genome copy number views established with WGS (upper panel) or with HiC seq (lower panel) for MP41 (A) and MP46 (B). Copy number status as normal, gains and losses are shown respectively in green, red and blue.

Supplementary Figure 9: Effect on compartment interaction scores after different normalization methods applied to HiC data generated for MP41, MP46 and NM. Log2 HiC interaction scores are depicted across copy number status defined at a 250kb window resolution. Interactions score generated on raw data, or after ICE, CAIC and LOIC normalization are compared for MP41 as respectively on A, B, C and D graphs, for MP46 as respectively on E, F, G and H graphs, and for NM as respectively on I, J , K, and L. Per boxplot graph, each color corresponds to a specific copy number.

Supplementary Figure 10: Normalization of HiC Data and comparison of compartment interaction scores per type of compartment, and interaction score distribution per copy number status and number of A/B compartments. From each normalization methods of HiC data generated for MP41, MP46 and NM, interactions scores for all compartments were separated on upon A/B status, and undefined status. Log2 HiC interaction scores are depicted across copy number status defined at a 250kb window resolution. Interactions score from raw data, or after ICE, CAIC and LOIC normalization are compared for MP41 as respectively on A, B, C and D graphs, for MP46 as respectively on E, F, G and H graphs, and for NM as respectively on I, J , K, and L. Per vignette, on the right panel a box plot details compartment interaction score per type of compartment, and copy number status, on the left panel an histogram quantifies number of interactions per type of compartment for each copy number status. Green, blue and grey box plots and bars corresponds respectively to euchromatin/ A compartment, heterochromatin/ B compartment, and not defined compartments.

Supplementary Figure 11: *PRAME* locus transcription factors (TF) upregulated in UM models. A. Hierarchical clustering of ENCODE enriched *PRAME – ZNF280A* TF. Blue stars indicate significantly upregulated TFs in MP41 and in MP46 vs NM. B. Comparison of absolute fold changes of significantly regulated *PRAME* TF. Absolute FC obtained in the MP41 vs NM comparisons and MP46 vs NM of regulated TFs binding the *PRAME* locus are plotted on the graph. TF are colored according the number of binding sites identified from ENCODE. C. 3 siRNAs selected to knock down gene *RAD21* and *PRAME* in MP41 cell line. D. MTT assay to evaluate cell viability and proliferation after 72h of RNA silencing in MP41. 3 biological replicate and 6 measurement per replicate were summarized in the graph. Four controls were included in the experiment: MP41 and lipofectamine without siRNA, 2 different negative siRNAs and a positive GAPDH siRNA control. Three different siRNA against *RAD21* (#25, 26 and 27) and 3 different siRNA against *PRAME* (#24, 25 and 26). All samples were normalized against average of MP41 and lipofectamine control. E. Western blot of RAD21, PRAME and GAPDH proteins. 100ng of protein lysates from a negative siRNA control, 3 *RAD21* siRNAs, 3 *PRAME* siRNA and a positive *GAPDH* control were loaded on a gel. 3 biological replicate were analyzed on western blot and quantifications were conducted with ImageLab. A relative quantification of protein of interest was carried out respect negative control and *GAPDH*.

Figure 1: Main characteristics of two PDXs established from aggressive uveal melanomas

A. Clinic features

Patient #1 :

- Woman diagnosed with localized uveal melanoma at 50 y/o
- Treatment: enucleation
- Phenotype: epithelioid
- Die at 53y/o, due to bones, lung, and subcutaneous metastasis

Patient #2 :

- Man diagnosed with localized uveal melanoma at 69y/o
- Treatment: enucleation
- Phenotype : epithelioid
- Die at 71y/o, due to liver metastasis

B. PDX characteristics

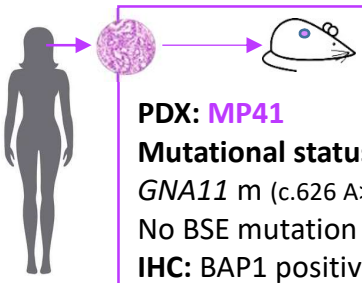

PDX: MP41
Mutational status:
GNA11 m (c.626 A>T)
No BSE mutation identified
IHC: BAP1 positive
CN analysis:
Monosomy 3, 6p+, 8q+

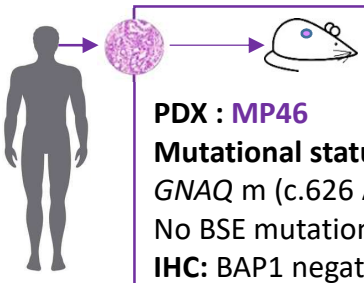

PDX : MP46
Mutational status:
GNAQ m (c.626 A >T)
No BSE mutation identified
IHC: BAP1 negative
CN analysis:
Isodisomy 3, 6p+, 8q+

BAP1 IHC on MP41 (40x)

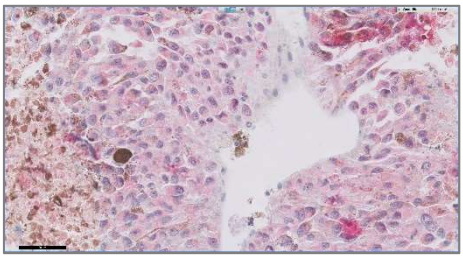

BAP1 IHC on MP46 (40x)

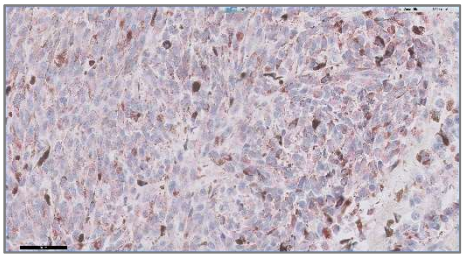

Figure 2: Gene expression global overview

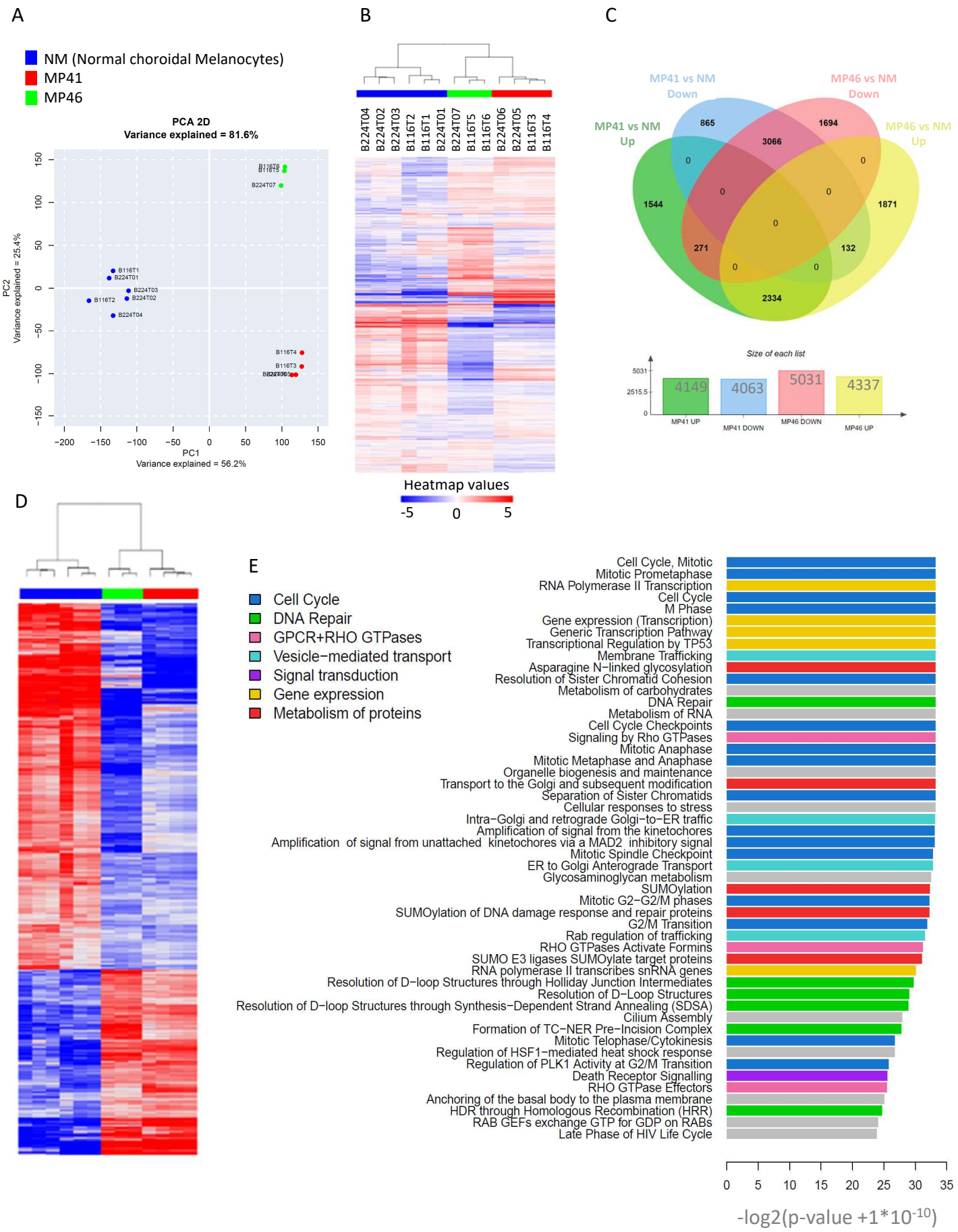

Figure 3: DNA optical mapping and multispectral FISH highlight chromosome aberrations and DNA rearrangements in MP41 and MP46.

A

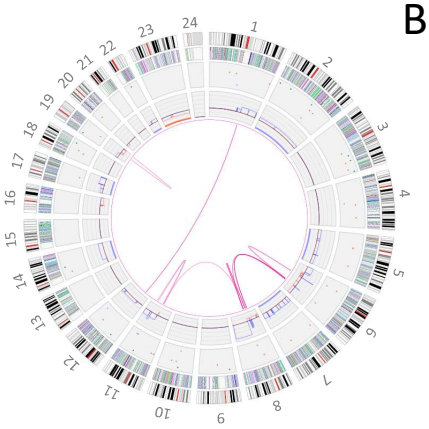

B

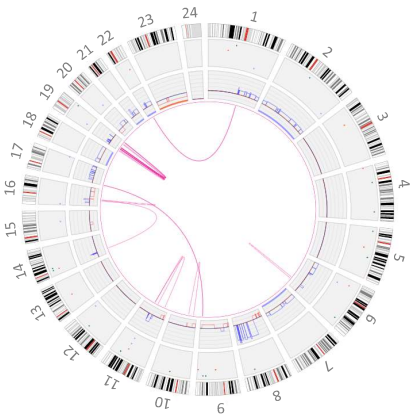

C

De novo assembly (hg19)	MP41 Counts	MP46 Counts
Insertion	14	19
Deletion	27	14
Inversion	2	1
Duplication	12	10
Intra-Translocation	8	14
Inter-Translocation	9	5

D

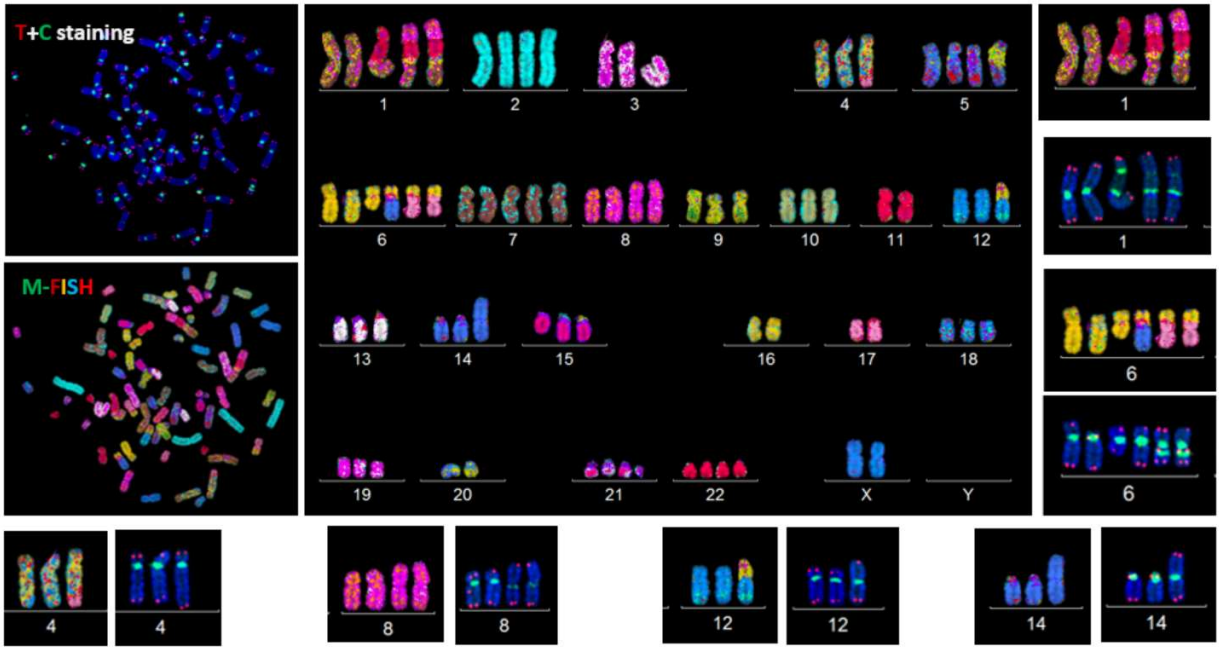

E

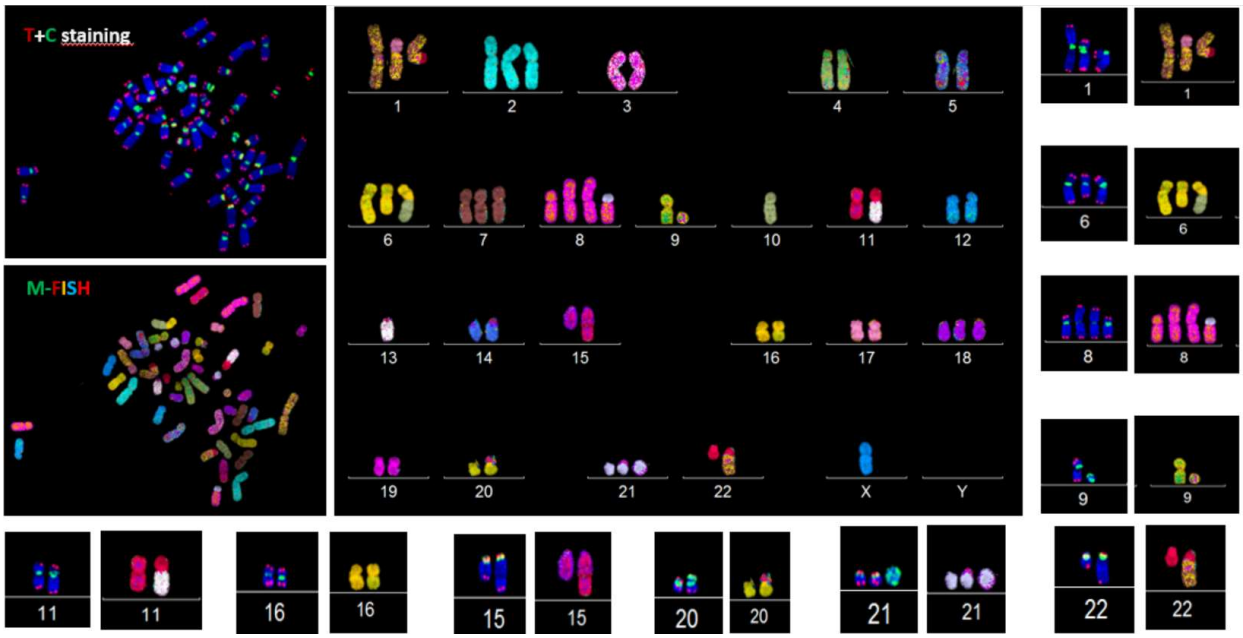

Figure 4: Whole genome DNA methylation reveals differences between UM models and Normal melanocytes

A

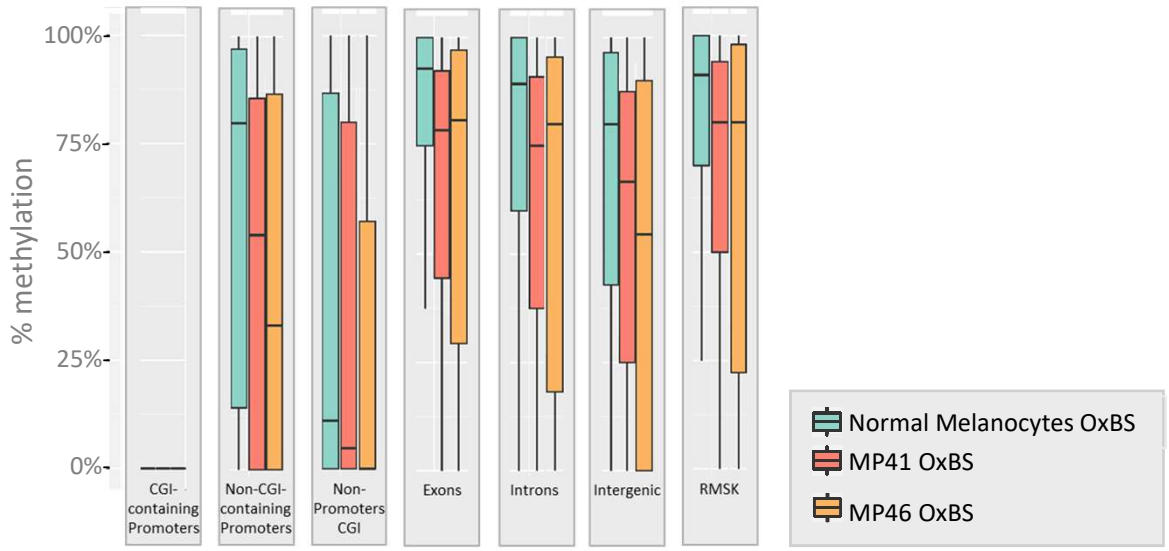

B

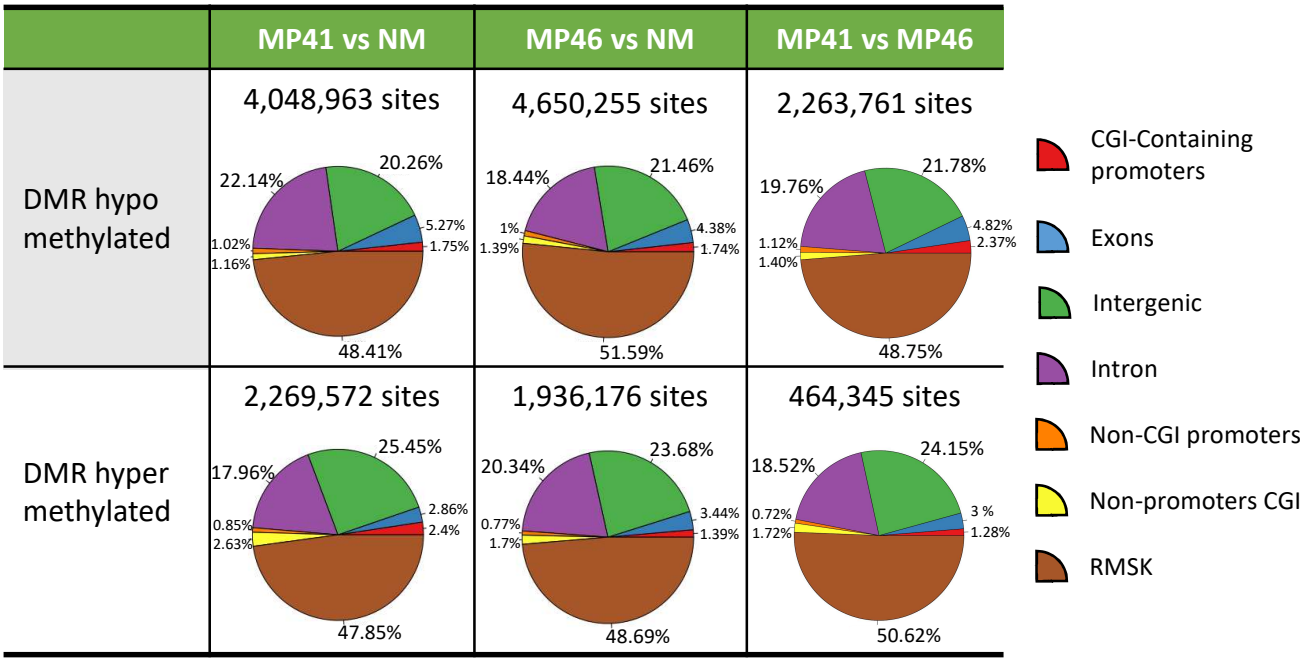

C *BAP1* methylation analysis revealed a 809 bp deletion in *BAP1/PHF7* promoter in MP46 (hg19, chr3:52,443,929-52,444,738)

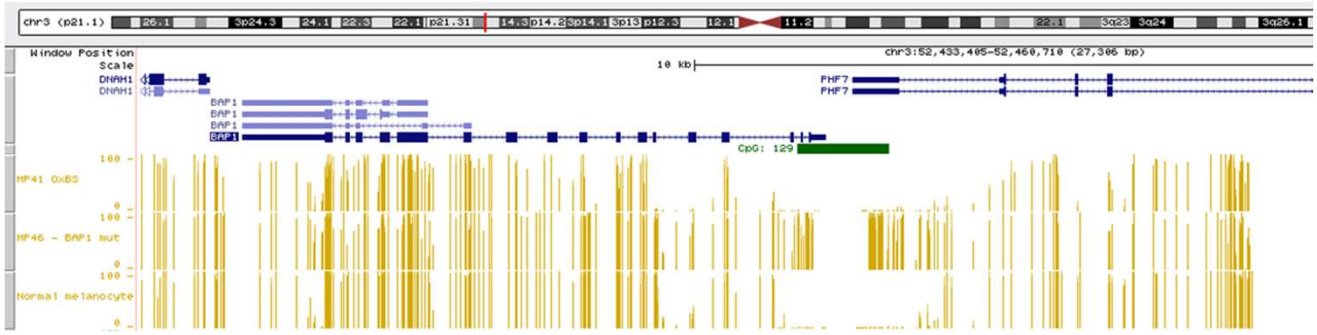

Figure 5 : Compartments and Topologically Associated Domains (TAD) in normal melanocytes and uveal melanoma models

A

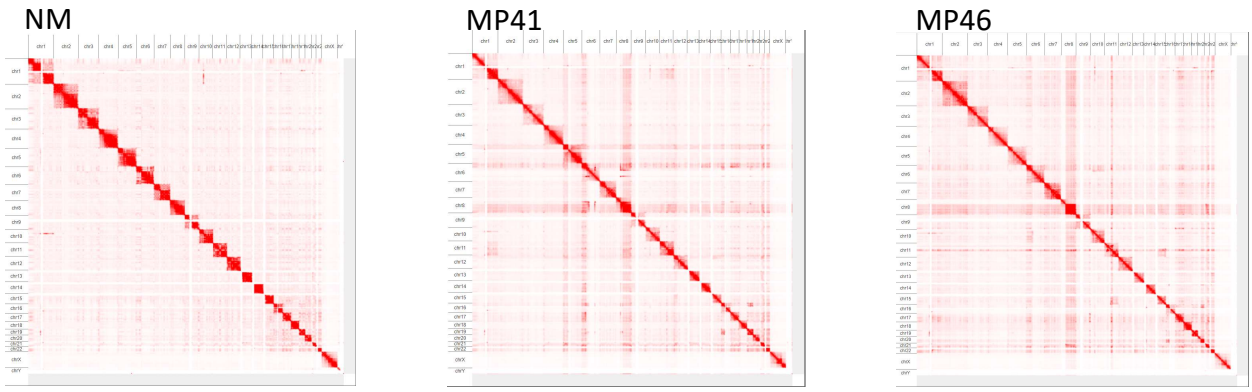

B Proportions of A/B compartment changes in NM, MP41 and MP46

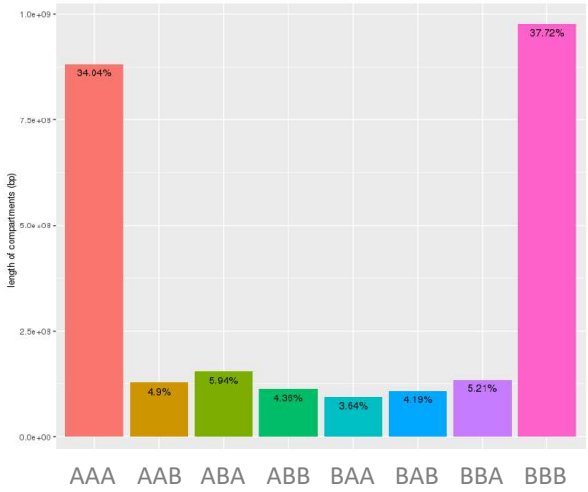

C Compartment changes and gene expression regulation in MP41, MP46 vs NM

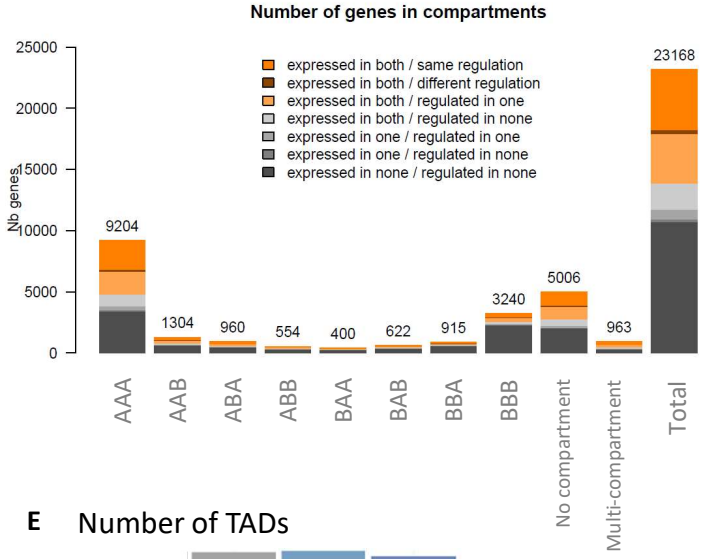

D Localization of inactivated (ABB) and activated (BAA) compartment MP41 and MP46 vs NM

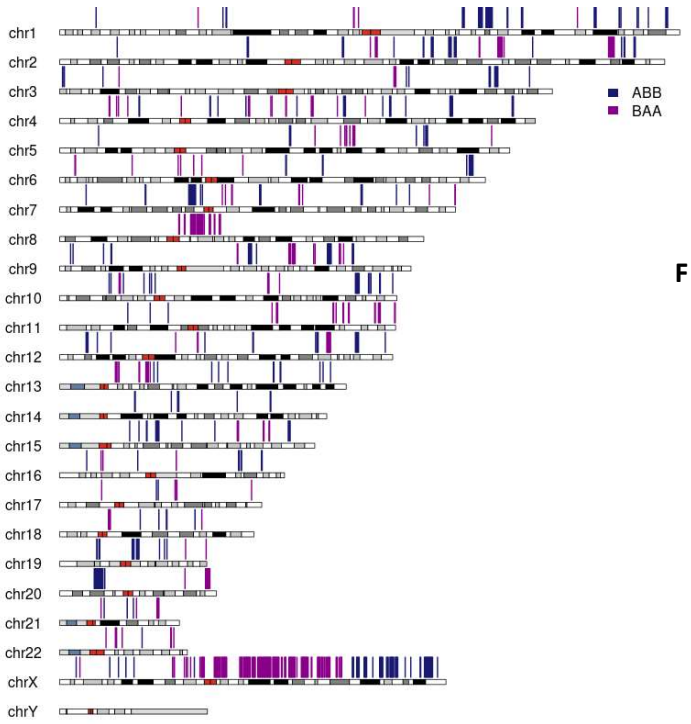

E Number of TADs

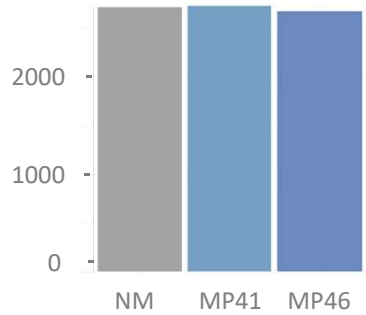

F Size of TADs

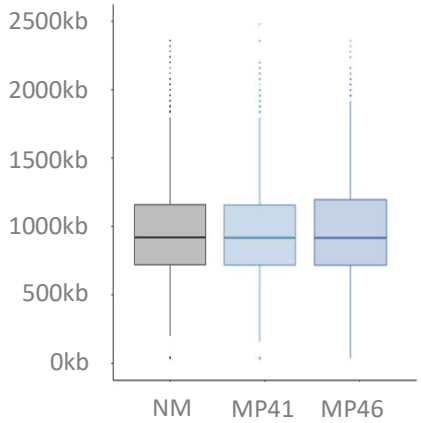

Figure 6: Multiomics analysis revealed a specific *Prame* activation pattern

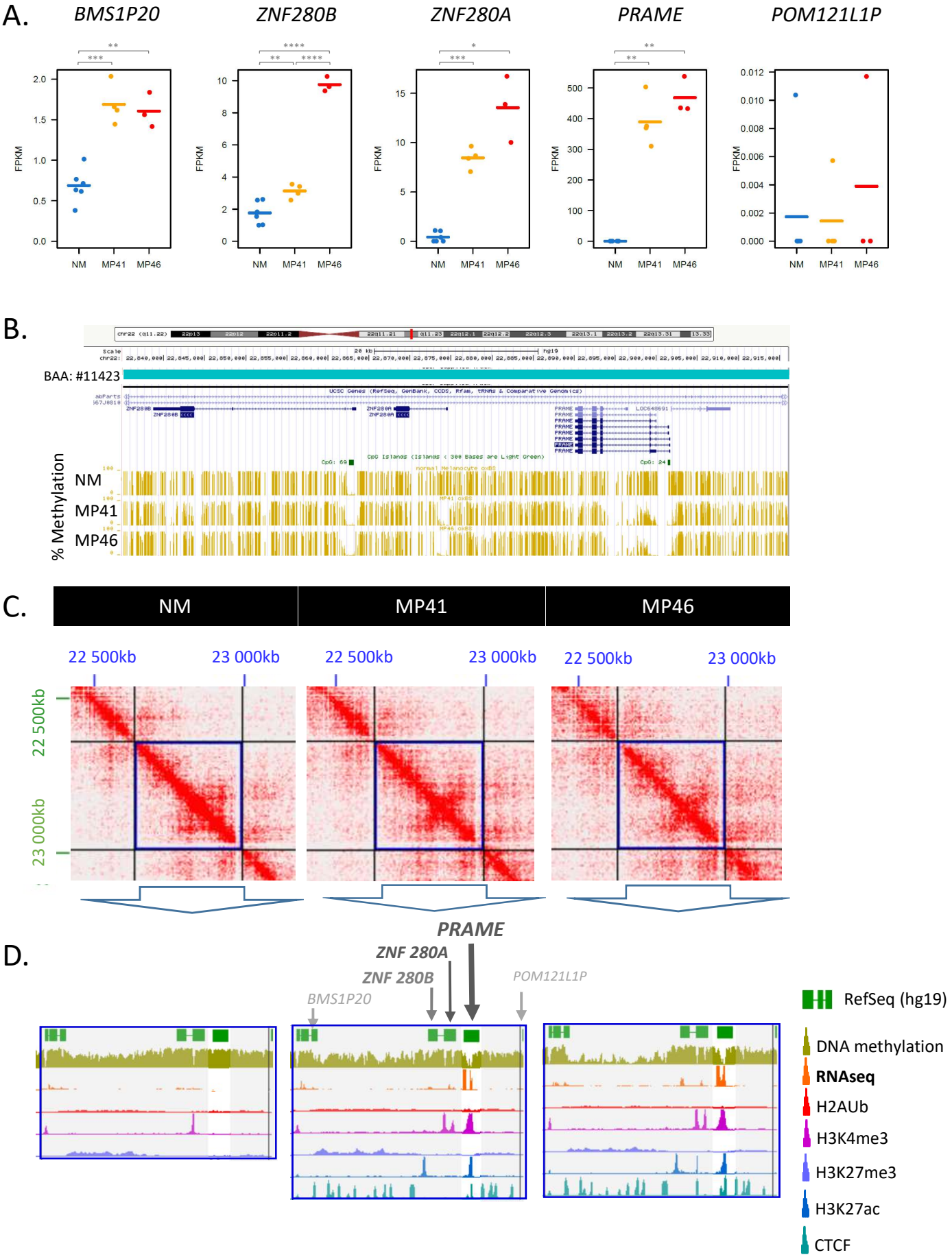

Table1 : Top 50 of regulated genes in UM models vs NM

Most regulated genes shared in the comparisons of MP41 vs Nm and MP46 vs NM are listed in 4 sub-tables. Gene are ranked according log 2 fold changes. A and B lists are the top 50 of regulated genes in MP41 vs NM and in MP46 vs NM. C and D tables are the top 30 of down regulated genes in MP41 vs Nm and MP46 vs NM. Genes written in bold are regulated with the same variation in both comparisons. Genes written in red were previously identified in UM studies.

A. Up regulated genes in MP41

Gene name	Ranked Log2FC in MP41	MP41 vs. NM: Log2FC	MP41 vs. NM: padj
HAGLR	**1**	**12.16**	**2.44E-63**
TRPM2-AS	**2**	**12.12**	**9.08E-29**
PRAME	**3**	**12.11**	**3.78E-138**
MT1M	**4**	**11.7**	**1.77E-25**
ASB11	**5**	**11.24**	**5.77E-55**
KLHL30	**6**	**10.73**	**8.10E-118**
NRN1	**7**	**10.56**	**2.21E-19**
TRPM2	**8**	**10.44**	**5.56E-16**
CCSER1	**9**	**9.98**	**9.12E-53**
RASGRP3	**10**	**9.96**	**1.95E-77**
HIF3A	**11**	**9.46**	**1.41E-57**
HOXA9 // HOXA10	**12**	**9.45**	**2.59E-87**
PAQR5	**13**	**9.38**	**7.74E-33**
LMX1B	**14**	**9.31**	**3.28E-30**
HOXA11	**15**	**9.29**	**8.02E-38**
EPHA4	**16**	**9.04**	**7.55E-124**
HOXC4 // HOXC5 // HOXC6	**17**	**8.91**	**1.65E-09**
IGLL3P	**18**	**8.79**	**4.08E-24**
LINC00482	**19**	**8.6**	**2.51E-103**
PGAM2	20	8.6	3.28E-182
PLCB4	21	8.59	1.43E-13
PNLDC1	**22**	**8.56**	**1.19E-99**
MAL2	**23**	**8.43**	**3.04E-24**
TTC39A	**24**	**8.17**	**1.72E-164**
SERPINB9P1	**25**	**8.01**	**1.98E-65**
RBP7	26	7.96	5.93E-21
LINC01531	**27**	**7.77**	**5.71E-106**
RAPGEF4	28	7.71	3.11E-39
SCIN	29	7.67	2.26E-82
TIAM2	30	7.64	1.21E-45
KIF17	31	7.6	3.03E-190
CACNA2D2	**32**	**7.58**	**6.51E-70**
EPHA8	**33**	**7.51**	**6.15E-53**
TWIST1	**34**	**7.46**	**2.18E-48**
LRRN2	**35**	**7.12**	**1.89E-38**
ENO3	36	7.04	0.00E+00
PITX2	**37**	**6.82**	**5.05E-19**
CYP26B1	**38**	**6.79**	**1.94E-35**
ITGB2	**39**	**6.67**	**7.50E-31**
GGT1	40	6.62	4.70E-89
SIX4	41	6.6	3.65E-33
VAMP8	42	6.58	7.33E-112
LTK	**43**	**6.57**	**1.09E-19**
GABRA3	**44**	**6.56**	**2.94E-05**
HIST1H2BC	45	6.47	8.04E-43
CHST9	46	6.47	1.11E-143
MGAT4A	**47**	**6.38**	**3.23E-44**
ART5	48	6.27	2.90E-97
WFDC1	49	6.21	5.25E-15
HAS2	**50**	**6.17**	**5.40E-44**

B. Up regulated genes in MP46

Gene name	Ranked Log2FC in MP46	MP46 vs. NM: Log2FC	MP46 vs. NM: padj
HAGLR	**1**	**12.48**	**3.56E-62**
PRAME	2	11.92	1.46E-113
HOXA9 // HOXA10	**3**	**10.85**	**9.40E-108**
RASGRP3	4	10.84	5.23E-77
MAL2	**5**	**10.6**	**2.43E-32**
ASB11	**6**	**10.59**	**3.51E-47**
PLCB4	7	10.28	3.01E-16
KLHL30	**8**	**10.16**	**9.85E-100**
HOXA11	**9**	**10.1**	**5.99E-42**
CCSER1	**10**	**9.74**	**1.10E-48**
LINC01531	**11**	**9.65**	**9.41E-141**
IGLL3P	**12**	**9.59**	**7.85E-26**
TKTL1	13	9.43	1.60E-34
TRPM2-AS	**14**	**9.33**	**3.29E-17**
RAPGEF4	15	9.09	5.34E-46
MT1M	**16**	**8.93**	**6.35E-15**
CYP26B1	**17**	**8.34**	**3.88E-49**
EPHA4	**18**	**8.1**	**5.07E-90**
LMX1B	**19**	**8.09**	**2.54E-22**
TWIST1	**20**	**8.01**	**1.59E-52**
HOXC4 // HOXC5 // HOXC6	**21**	**7.75**	**1.82E-06**
TRPM2	**22**	**7.73**	**5.83E-08**
NRN1	**23**	**7.68**	**3.35E-09**
EPHA8	**24**	**7.52**	**1.83E-48**
HIF3A	**25**	**7.48**	**1.31E-34**
TTC39A	**26**	**7.42**	**2.68E-120**
ITGB2	**27**	**7.37**	**5.36E-32**
LRRC39	28	7.25	1.86E-80
PAQR5	**29**	**7.14**	**7.21E-19**
PITX2	**30**	**6.89**	**1.88E-16**
AFDN	31	6.78	2.02E-32
SERPINB9P1	**32**	**6.69**	**2.66E-41**
LTK	**33**	**6.55**	**1.25E-16**
TEX14	34	6.5	1.05E-84
STUM	35	6.45	3.56E-19
LINC00482	**36**	**6.4**	**1.90E-49**
KCNE3	37	6.32	1.47E-20
HAS2	**38**	**6.32**	**8.15E-39**
SLC9A3	39	6.29	2.91E-50
REREP3	40	6.27	7.93E-05
GABRA3	**41**	**6.21**	**2.80E-04**
PNLDC1	**42**	**6.2**	**2.55E-46**
CACNA2D2	**43**	**6.09**	**1.45E-38**
IGFBPL1	44	5.95	4.69E-43
PNMA3	45	5.93	7.32E-70
LRRN2	**46**	**5.93**	**1.01E-22**
FAM174B	47	5.8	1.45E-26
TMEM200C	48	5.78	7.37E-04
AMN	49	5.72	2.49E-44
MGAT4A	**50**	**5.71**	**7.25E-30**

C. Down regulated genes in MP41

Gene name	Ranked Log2FC	MP41 vs. NM: Log2FC	MP41 vs. NM: padj
CYBRD1	1	-11.6	3.65E-87
LEF1	2	-11.11	6.43E-60
GPR173	3	-11	1.76E-34
CPQ	4	-10.8	2.38E-135
NLGN1	5	-10.62	7.67E-21
DPP6	6	-10.15	2.66E-48
TNFRSF10D	7	-9.88	5.46E-25
FAM50B	8	-9.78	9.53E-51
IGFBP5	9	-9.75	4.84E-61
ZNF667	**10**	**-9.6**	**2.32E-44**
MAP1B	11	-9.45	1.80E-97
ANTXR1	12	-9.12	8.38E-78
FN1	13	-8.95	4.30E-96
UCHL1	14	-8.83	3.23E-32
CHL1	15	-8.81	7.66E-50
SLC35G2	16	-8.79	2.97E-24
LHFPL3-AS1	17	-8.79	2.24E-41
ANGPTL2	18	-8.77	1.10E-38
NR2F1	19	-8.66	7.40E-14
PRUNE2	20	-8.65	2.81E-133
NTNG1	21	-8.58	4.33E-48
NAALAD2	22	-8.52	1.39E-11
GFRA3	**23**	**-8.52**	**1.13E-13**
ABCA8	**24**	**-8.4**	**2.02E-47**
SCN1B	**25**	**-8.31**	**5.38E-97**
ADCY1	26	-8.28	3.23E-123
OCIAD2	27	-8.16	8.44E-13
PMEPA1	**28**	**-8.13**	**2.64E-72**
FAM19A5	**29**	**-8.1**	**1.39E-65**
KNDC1	30	-8.06	6.37E-30
MBNL3	31	-7.88	1.23E-11
RBMS3	32	-7.81	1.30E-14
NID1	33	-7.79	1.95E-92
JAM3	34	-7.72	9.59E-105
CHST2	35	-7.61	2.30E-76
HS3ST1	**36**	**-7.56**	**3.29E-21**
SLITRK2	37	-7.54	3.14E-51
SCD5	38	-7.53	1.09E-107
SGCE	39	-7.53	1.39E-65
GABRG3	40	-7.51	1.09E-32
CTSK	41	-7.49	4.27E-157
PXDN	42	-7.39	6.48E-41
SLCO3A1	43	-7.38	1.28E-57
SDC2	44	-7.29	6.87E-52
IGFBP7	45	-7.24	2.93E-51
TMEM169	46	-7.22	1.49E-31
SLC15A3	47	-7.17	2.62E-91
DCLK1	48	-7.16	3.13E-26
MGMT	**49**	**-7.11**	**1.78E-28**
HCN2	50	-7.07	3.72E-74

D. Down regulated genes in MP46

Top 30 MP46 vs NM	Ranked Log2 FC : MP46 vs NM	MP46 vs. NM: Log2FC	MP46 vs. NM: padj
BAP1	1	-14.48	3.63E-57
SFRP1	2	-12.45	4.49E-59
FAM19A5	**3**	**-12.13**	**1.92E-49**
HLA-C	4	-11.2	9.73E-41
PALM	5	-10.63	2.15E-59
PCSK1N	6	-10.59	1.34E-34
PTPRH	7	-10.37	2.19E-23
HS3ST1	8	-10.2	2.13E-15
SLFN12	9	-9.95	2.07E-19
ABCA8	10	-9.91	3.14E-43
TTYH1	11	-9.8	6.83E-10
APOBEC3C	12	-9.67	4.70E-87
FAM171A1	13	-9.64	9.61E-14
IL27RA	14	-9.4	1.19E-30
PRKCB	15	-9.26	1.63E-46
SLAMF9	16	-9.21	3.95E-08
LINC01443	17	-9.17	4.76E-14
ANXA1	18	-9.01	1.03E-29
ZNF667	**19**	**-8.96**	**1.89E-50**
MGMT	**20**	**-8.86**	**7.47E-35**
SYT5	21	-8.82	1.14E-07
FCRLA	22	-8.81	9.90E-39
LINC01314	23	-8.75	2.17E-41
GFRA3	**24**	**-8.56**	**1.58E-13**
EHD2	25	-8.51	3.04E-78
SCN1B	**26**	**-8.45**	**2.62E-86**
DHH	27	-8.43	1.40E-12
PMEPA1	**28**	**-8.43**	**1.34E-64**
PSMB9	29	-8.29	6.33E-41
CA11	30	-8.19	6.18E-41
S100B	31	-8.05	4.45E-50
FAM198B	32	-7.99	8.75E-120
ST8SIA1	33	-7.83	5.42E-37
FXYD1	34	-7.83	6.47E-42
DLGAP1	35	-7.83	3.56E-30
NPTX1	36	-7.82	2.37E-14
CLEC11A	37	-7.76	1.09E-91
PLP2	38	-7.75	1.64E-86
ITGAX	39	-7.68	4.03E-31
FOSL1	40	-7.6	1.73E-71
FLRT3	41	-7.6	1.79E-64
KRT17	42	-7.59	7.70E-15
DLX1	43	-7.55	5.08E-42
UBE2L6	44	-7.5	6.03E-51
PRELP	45	-7.45	4.23E-96
TIMP1	46	-7.4	4.84E-69
ECM1	47	-7.34	7.72E-60
LGI4	48	-7.33	1.18E-42
CCDC184	49	-7.3	4.34E-30
TGFB1	50	-7.29	1.45E-48